



## Impacts of niobia loading on active sites and surface acidity in $\text{NbO}_x/\text{CeO}_2\text{--ZrO}_2$ $\text{NH}_3\text{--SCR}$ catalysts

Ziran Ma<sup>a</sup>, Xiaodong Wu<sup>b,\*</sup>, Zhichun Si<sup>c</sup>, Duan Weng<sup>a,c, \*\*</sup>, Jing Ma<sup>b</sup>, Tengfei Xu<sup>a</sup>

<sup>a</sup> State Key Laboratory of New Ceramics & Fine Process, School of Materials Science and Engineering, Tsinghua University, Beijing 100084, China

<sup>b</sup> The Key Laboratory of Advanced Materials of Ministry of Education, School of Materials Science and Engineering, Tsinghua University, Beijing 100084, China

<sup>c</sup> Advanced Materials Institute, Graduate School at Shenzhen, Tsinghua University, Shenzhen 518055, China

### ARTICLE INFO

#### Article history:

Received 12 February 2015

Received in revised form 24 April 2015

Accepted 18 May 2015

Available online 19 May 2015

#### Keywords:

Niobia

$\text{CeO}_2\text{--ZrO}_2$

Electronic interaction

Surface acidity

$\text{NH}_3\text{--SCR}$

### ABSTRACT

A series of  $\text{NbO}_x/\text{Ce}_{0.75}\text{Zr}_{0.25}\text{O}_2$  catalysts for the selective catalytic reduction of NO with ammonia ( $\text{NH}_3\text{--SCR}$ ) were synthesized using a wetness impregnation method. The effect of niobia loading was studied in relation to the active sites and surface acidity.  $\text{NH}_3/\text{NO}$  oxidation, X-ray diffraction, Infrared spectroscopy, ultraviolet-visible spectroscopy, X-ray photoelectron spectroscopy,  $\text{H}_2$  temperature-programmed reduction,  $\text{O}_2/\text{NH}_3$  temperature-programmed desorption, and diffuse reflectance infrared Fourier transformed spectroscopy experiments were performed to correlate the catalyst structure and surface properties to catalytic performance after  $\text{Nb}_2\text{O}_5$  modification. The catalyst with 15 wt.%  $\text{Nb}_2\text{O}_5$  loading showed high  $\text{NH}_3\text{--SCR}$  activity and nearly 100%  $\text{N}_2$  selectivity within a broad operation temperature window (190–460 °C) at a high space velocity (300,000  $\text{h}^{-1}$ ). On this catalyst,  $\text{Nb}^{n+}$  was mainly distributed in the form of typical monomeric and polymeric  $\text{NbO}_x$  species, and was partially incorporated into the  $\text{Ce}_{0.75}\text{Zr}_{0.25}\text{O}_2$  lattice at the  $\text{Nb}^{n+}\text{--O--Ce}^{n+}$  ( $\text{Zr}^{n+}$ ) interface. The electron redistribution effect arising from the occupation of cerium sites by  $\text{Nb}^{n+}$  ions promoted the formation of  $\text{Ce}^{3+}$  ions, oxygen vacancies and active oxygen species. This interaction was closely associated with the distribution of  $\text{NbO}_x$  species which varied with niobia loading.  $\text{NbO}_x$  themselves were acid sites and by attracting electrons they enhanced Lewis acid sites on CZ surface, which promoted the adsorption of  $\text{NH}_3$  and inhibited the unselective oxidation of  $\text{NH}_3$  to  $\text{NO}_x$ . The increased amounts of active oxygen species over NbCZ catalysts promoted the adsorptive oxidation of  $\text{NH}_3$  to  $\text{NH}_2$  and  $\text{NO}$  to  $\text{NO}_3^-$  at low temperatures, and thus facilitated the reaction of ads- $\text{NH}_3$  and ads- $\text{NO}_3^-/\text{NO}_2^-$  species. This effect as well as the increased amount of acid sites led to good  $\text{NH}_3\text{--SCR}$  performance of Nb15CZ in a wide temperature range.

© 2015 Elsevier B.V. All rights reserved.

## 1. Introduction

Nitrogen oxides ( $\text{NO}_x$ ) emitted from stationary boilers and mobile engines lead to various environmental problems, e.g. acid rain, photochemical smog, ozone depletion and greenhouse effect [1–3]. Due to the strong polluting effects of nitrogen oxides, regulations of emission levels are becoming ever more stringent, especially in Europe, Japan, the United States [1] and China [4]. Among the various treatment techniques that have been proposed

or developed for  $\text{NO}_x$  abatement, the selective catalytic reduction (SCR) using ammonia as a reductant in the oxygen-rich exhausts is the most efficient way to fulfill this task [1–3]. Nowadays, the well-studied types of catalysts in  $\text{NO}_x$  removal are  $\text{V}_2\text{O}_5/\text{WO}_3$  ( $\text{MoO}_3$ )– $\text{TiO}_2$  and transition-metal exchanged zeolites [2,3,5–7]. However, some drawbacks remain for vanadium-based catalysts, including the narrow operation temperature window, the toxicity and volatility of  $\text{V}_2\text{O}_5$  species and the easy transformation of the  $\text{TiO}_2$  support from anatase to rutile at high temperature. On the other hand, although zeolites catalysts show as potential substitutes of vanadium-based catalysts, the durability to severe thermal deactivation induced by combustion of stored HCs is still unsatisfactory [5–7]. Generally,  $\text{NH}_3\text{--SCR}$  catalysts in diesel engines should provide several specific catalytic properties, such as satisfactory  $\text{NH}_3\text{--SCR}$  performance in a considerable wide temperature window, high durability to chemical impurities poisoning from the exhaust gases, and ultra-high hydrothermal stability to resist timed

\* Corresponding author. Tel.: +86 10 62792375.

\*\* Corresponding author at: State Key Laboratory of New Ceramics & Fine Process, School of Materials Science and Engineering, Tsinghua University, Beijing 100084, China. Tel.: +86 10 62785986.

E-mail addresses: [wuxiaodong@tsinghua.edu.cn](mailto:wuxiaodong@tsinghua.edu.cn) (X. Wu), [duanweng@tsinghua.edu.cn](mailto:duanweng@tsinghua.edu.cn) (D. Weng).

thermal shock induced by the regeneration of diesel particulate filters (DPF) installed upstream of the SCR convertor [1–3,7]. Therefore, it is imperative to develop novel vanadium-free catalysts with high deNO<sub>x</sub> activity, high N<sub>2</sub> selectivity, excellent hydrothermal stability, and insensitivity to exhaust components poisoning such as HC, SO<sub>2</sub> and alkali metals.

Ceria, considered as a very active oxide in the SCR reaction, possesses considerable oxygen storage capacity owing to the redox cycling between Ce<sup>3+</sup> and Ce<sup>4+</sup>, which has been already widely used as a crucial component in three-way catalysts (TWCs). Its acid-base properties, lack of toxicity and low cost also attract much attention. Recently, much research has been focused on the ceria-based NH<sub>3</sub>–SCR catalysts, such as CeO<sub>2</sub>–TiO<sub>2</sub> [8–10], CeO<sub>2</sub>–WO<sub>3</sub> [11–18], CeO<sub>2</sub>–SO<sub>4</sub><sup>2-</sup> [19–21], CeO<sub>2</sub>–Nb<sub>2</sub>O<sub>5</sub> [22–26], CeO<sub>2</sub>–PO<sub>4</sub><sup>3-</sup> [27,28] and CeO<sub>2</sub>–MoO<sub>3</sub> [29,30]. The SCR performance of ceria-based catalysts could be remarkably enhanced by introducing solid acid components such as tungsta, niobia, phosphate and sulfate, which mainly due to both excellent redox ability and strong acidity. Among them, CeO<sub>2</sub>–Nb<sub>2</sub>O<sub>5</sub> based catalysts appear to be a more promising candidate for diesel after-treatment systems due to its multifunctionality, such as (1) the SCR of NO with NH<sub>3</sub>, (2) the hydrolysis of urea to NH<sub>3</sub> and (3) the oxidation of soot [23,24]. It has been reported that the addition of Nb<sub>2</sub>O<sub>5</sub> could promote the acidity of the catalysts due to the acidic nature of NbO<sub>x</sub> species [22–25]. Furthermore, the fact that amount of chemical defects (oxygen vacancies) in Nb–Ce mixed oxides is increased after Nb doping, which is confirmed by the concomitant increase in electron conductivity, has been revealed in some studies [31,32]. However, despite some studies on SCR performance in different reaction conditions, the comprehensive study in structure–activity relationship of CeO<sub>2</sub>–Nb<sub>2</sub>O<sub>5</sub> based catalysts is still lacking, e.g. the correlation of deNO<sub>x</sub> activity to surface acidity and redox ability. In our previous study [26], a significantly enhanced activity for NO<sub>x</sub> reduction was attained by addition of Nb<sub>2</sub>O<sub>5</sub> into CeO<sub>2</sub>–WO<sub>x</sub>/TiO<sub>2</sub> catalyst, which is due to the synergistic effect between Ce and Nb.

Considering the redox property and thermal stability [28,33,34], Ce<sub>0.75</sub>Zr<sub>0.25</sub>O<sub>2</sub> mixed oxides with a Ce/Zr mole ratio of 3:1 was chosen as a ceria based support in this work. Various characterizations related to the structure, adsorption and redox properties of NbO<sub>x</sub>/Ce<sub>0.75</sub>Zr<sub>0.25</sub>O<sub>2</sub> catalysts were performed aiming to elucidate this relationship. We also present a primary scheme regarding to the correlation between deNO<sub>x</sub> performance, surface acidity and redox property modulated by Nb<sub>2</sub>O<sub>5</sub> content.

## 2. Experimental

### 2.1. Catalyst preparation

Ce<sub>0.75</sub>Zr<sub>0.25</sub>O<sub>2</sub> (CZ) powder was synthesized by a sol–gel method using Ce(NO<sub>3</sub>)<sub>4</sub>·6H<sub>2</sub>O and Zr(NO<sub>3</sub>)<sub>4</sub>·5H<sub>2</sub>O as the precursors. Citric acid was used as the complexing agent. Precursor salts, citric acid, and deionized water were mixed at a mole ratio of 1:2:100. The mixed solution was magnetically stirred in a water bath at 80 °C until a spongy yellow gel was formed. The gel was dried at 110 °C in an oven overnight. The resulting product was subsequently subjected to decomposition at 300 °C for 1 h and calcination at 550 °C for 3 h in a muffle and finally ground to a fine powder. The NbO<sub>x</sub>/Ce<sub>0.75</sub>Zr<sub>0.25</sub>O<sub>2</sub> (NbCZ) catalysts were synthesized by impregnating the as-received Ce<sub>0.75</sub>Zr<sub>0.25</sub>O<sub>2</sub> powders with C<sub>12</sub>H<sub>7</sub>NbO<sub>24</sub> solution. The nominal loadings of niobia (calculated in Nb<sub>2</sub>O<sub>5</sub>) were 5 wt.%, 10 wt.%, 15 wt.% and 20 wt.%, respectively, which were denoted as Nb(x)CZ with x representing the mass percentage of Nb<sub>2</sub>O<sub>5</sub>. The impregnated powders were dried at 110 °C overnight and calcined at 550 °C for 3 h in static air. For comparison, the pure Ce<sub>0.75</sub>Zr<sub>0.25</sub>O<sub>2</sub> (CZ) powders also underwent the same thermal

treatment. In some characterizations, Nb<sub>2</sub>O<sub>5</sub> was also used as reference; in this case it was prepared by calcination of a C<sub>12</sub>H<sub>7</sub>NbO<sub>24</sub> precursor at 600 °C for 4 h. The conventional V<sub>2</sub>O<sub>5</sub>/WO<sub>3</sub>–TiO<sub>2</sub> catalyst was also prepared by impregnating 1 wt.% V<sub>2</sub>O<sub>5</sub> on the 10 wt.% WO<sub>3</sub>–TiO<sub>2</sub> mixed oxides.

The as-received Nb15CZ catalyst was treated in 10% H<sub>2</sub>O/air at 760 °C for 24 h and denoted as the hydrothermally aged catalyst (A-Nb15CZ). Sulfur poisoning of Nb15CZ was performed in 100 ppm SO<sub>2</sub> + 10% H<sub>2</sub>O/air at 400 °C for 24 h, and the obtained sample was denoted as the sulfur poisoned catalyst (S-Nb15CZ).

### 2.2. Activity measurement

The NH<sub>3</sub>–SCR activity measurement was carried out in a fixed-bed quartz reactor with the effluent gases monitored by Thermo Nicolet 380 FTIR spectrometer. Samples of 200 mg (0.1 ml) sieved to 40–80 mesh were used for evaluation under the following conditions: 500 ppm NO, 500 ppm NH<sub>3</sub>, 5% O<sub>2</sub>, 12% CO<sub>2</sub>, 5% H<sub>2</sub>O (when used), N<sub>2</sub> as balance, 500 ml min<sup>-1</sup> total flow rate, and GHSV = 3 × 10<sup>5</sup> h<sup>-1</sup>. The inlet and outlet gas pipes were maintained above 150 °C to prevent formation and deposition of ammonium nitrates. The measurement was performed with 50 degrees stepwise ranging from 100 to 500 °C. The NH<sub>3</sub>–SCR activity, N<sub>2</sub> selectivity and the pseudo-first order rate constant (k) of catalysts were calculated as follows (Eqs. (1–3). In Eq. (3), F was the total flow rate, W the weight of catalyst and X the NO<sub>x</sub> conversion of the catalyst [13,25].

$$\text{NO}_x \text{ conversion (\%)} = \left( 1 - \frac{[\text{NO}]_{\text{out}} + [\text{NO}_2]_{\text{out}}}{[\text{NO}]_{\text{in}}} \right) \times 100 \quad (1)$$

$$\text{N}_2 \text{ selectivity (\%)} = \left( 1 - \frac{[\text{NO}_2]_{\text{out}} + 2 \times [\text{N}_2\text{O}]_{\text{out}}}{[\text{NH}_3]_{\text{in}} + [\text{NO}]_{\text{in}} - [\text{NH}_3]_{\text{out}} - [\text{NO}]_{\text{out}}} \right) \times 100 \quad (2)$$

$$k = - \frac{F}{W} \ln(1 - X) \quad (3)$$

NH<sub>3</sub>/NO oxidation experiments were performed under similar conditions as the SCR reaction, except that either NO or NH<sub>3</sub>, respectively, was excluded from the gas mixture. The NH<sub>3</sub> conversion was calculated based on Eq. (4). The selectivity to N<sub>2</sub> in the NH<sub>3</sub> oxidation was estimated based on the nitrogen balance (Eq. (5)) [13].

$$\text{NH}_3 \text{ conversion (\%)} = \left( 1 - \frac{[\text{NH}_3]_{\text{out}}}{[\text{NH}_3]_{\text{in}}} \right) \times 100 \quad (4)$$

$$\text{N}_2 \text{ selectivity (\%)} = \left( 1 - \frac{2[\text{N}_2\text{O}]_{\text{out}} + [\text{NO}]_{\text{out}} + [\text{NO}_2]_{\text{out}}}{[\text{NH}_3]_{\text{in}} - [\text{NH}_3]_{\text{out}}} \right) \times 100 \quad (5)$$

### 2.3. Catalyst characterization

X-ray diffraction (XRD) experiments were performed on a Shimadzu s-7000 diffractometer (Japan) employing Cu K $\alpha$  radiation ( $\lambda = 0.15418$  nm) operated at 40 kV and 120 mA. The X-ray diffractogram was recorded at 0.02° intervals in range of 20° ≤ 2θ ≤ 80° with a scanning velocity of 4° min<sup>-1</sup>. The crystalline phases were identified using JCPDS (Joint Committee on Powder Diffraction Standards) cards.

Nitrogen adsorption isotherms were measured on a JW-BK122F (JWGB, China) instrument. All the samples were degassed at 220 °C for 1 h prior to the nitrogen adsorption measurements. The BET surface area was determined by a multipoint BET method,

using the adsorption data in the relative pressure ( $P/P_0$ ) range of 0.05–0.3. The adsorption branch of nitrogen adsorption-desorption isotherms was used to determine the pore size distribution by the Barret–Joyner–Halender (BJH) method, assuming a cylindrical pore model. The surface Nb density ([atom] nm<sup>-2</sup>) was determined as the ratio of the number of Nb atoms and actual  $S_{\text{BET}}$  of the Ce<sub>0.75</sub>Zr<sub>0.25</sub>O<sub>2</sub> component, as shown in Eq. (6).

#### Surface density

$$= \frac{12.04 \times 10^5 \times (x) \text{ wt.\%}}{M(\text{Nb}_2\text{O}_5) \times S_{\text{BET}}(\text{Ce}_{0.75}\text{Zr}_{0.25}\text{O}_2) \times (1 - (x) \text{ wt.\%})} \quad (6)$$

Raman spectra were obtained with a LabRAM HR 800 (HORIBA Jobin Yvon, France) spectrometer at room temperature and atmospheric pressure. A wavelength of 633 nm was used for the exciting source from an argon ion laser. The laser beam was focused onto an area 0.1 × 0.1 mm<sup>2</sup> in size of the sample surface. The wavenumber values of the Raman spectra were accurate to 1 cm<sup>-1</sup>.

IR spectra of samples were collected on a Thermo Nicolet 6700 FTIR spectrometer equipped with a Smart ART appendix. The spectral resolution was 4 cm<sup>-1</sup>.

The UV-vis spectra (UV-vis) were measured in diffuse reflectance mode using a Shimadzu UV-2100S spectrometer (Japan) equipped with an internal integration sphere. A BaSO<sub>4</sub> pellet was used as a reference. The spectra were recorded at room temperature in the spectral range 200–800 nm.

X-ray photoelectron spectroscopy (XPS) data were obtained with experiments on a PHI-Quantera SXM system (Japan) equipped with monochromatic Al K $\alpha$  X-rays under UHV ( $6.7 \times 10^{-8}$  Pa). Sample charging effects were eliminated by correcting the observed spectra with a C-1s binding energy (BE) value of 284.6 eV from adventitious carbon.

H<sub>2</sub> temperature-programmed reduction (H<sub>2</sub>-TPR) was performed on Micromeritics AutoChem II 2920 (USA). Prior to H<sub>2</sub>-TPR experiment, the 100 mg sample was treated with 2% O<sub>2</sub>/He with 50 ml min<sup>-1</sup> flow at 500 °C for 30 min. The reactor was heated from room temperature to 1000 °C at a rate of 10 °C min<sup>-1</sup> in 10% H<sub>2</sub>/Ar flow (50 ml min<sup>-1</sup>).

Temperature-programmed desorption of oxygen (O<sub>2</sub>-TPD) measurements were performed in a fixed-bed quartz reactor with the effluent gases monitored using a quadrupole mass spectrometer (MS) (Omnistar 200). The 100 mg sample was pretreated in a He flow at 200 °C for 1 h. Then the catalyst was saturated with O<sub>2</sub> (50 ml min<sup>-1</sup>) for 30 min at room temperature and purged with He flow (300 ml min<sup>-1</sup>) for 30 min. The sample was heated to 900 °C from room temperature with a 10 °C min<sup>-1</sup> ramp in He flow (50 ml min<sup>-1</sup>).

A similar process was adopted for temperature-programmed desorption of NH<sub>3</sub> (NH<sub>3</sub>-TPD) with a Thermo Nicolet 380 FTIR spectrometer as a detector. Prior to the experiment, the 100 mg sample was pretreated at 500 °C with a gas flow of 5% O<sub>2</sub>/N<sub>2</sub> for 30 min. Then the samples were cooled down to 100 °C and exposed to NH<sub>3</sub> until saturation was reached, followed by flushing with N<sub>2</sub> at the same temperature to avoid physisorption of NH<sub>3</sub>. Afterwards, the NH<sub>3</sub>-saturated samples were cooled down to 50 °C and then ramped to 500 °C at a heating rate of 10 °C min<sup>-1</sup> in N<sub>2</sub>.

DRIFTS spectra of adsorbed species arising from NH<sub>3</sub> adsorption at various temperatures, were recorded in the range of 4000–650 cm<sup>-1</sup> using a Thermo Nicolet 6700 FTIR spectrometer. The sample in a diffuse reflectance IR cell was purged by N<sub>2</sub> (100 ml min<sup>-1</sup>) at 500 °C for 30 min to remove traces of organic residues. Then the sample was cooled down to 20 °C, exposed to 1000 ppm NH<sub>3</sub>/N<sub>2</sub> (100 ml min<sup>-1</sup>) for 1 h, and subsequently flushed with N<sub>2</sub>. Afterwards, the DRIFTS spectra of catalysts were collected at various temperatures. Further, NO + O<sub>2</sub> co-adsorption or

NO + NH<sub>3</sub> + O<sub>2</sub> reaction were carried out, in which the feeding gas of 1000 ppm NO + 10% O<sub>2</sub> or 1000 ppm NO + 1000 ppm NH<sub>3</sub> + 10% O<sub>2</sub> was continuously introduced to the N<sub>2</sub>-pretreated sample.

## 3. Results

### 3.1. Catalytic activities of catalysts

#### 3.1.1. SCR reaction

The NH<sub>3</sub>-SCR activities of catalysts are shown in Fig. 1a. The N<sub>2</sub> selectivity considering the formation of NO<sub>2</sub> and N<sub>2</sub>O as byproducts in the SCR reaction is presented in Fig. 1b. CZ shows poor activity within the whole temperature range investigated, with the maximum NO<sub>x</sub> conversion of only about 50%. The NO<sub>x</sub> conversion drops rapidly after peaking at 300 °C and even becomes negative above 400 °C as a result of pronounced production of NO<sub>2</sub>. Meanwhile, its selectivity to N<sub>2</sub> decreases from 90% at 300 °C to 75% at 450 °C. With Nb<sub>2</sub>O<sub>5</sub> loading amount increasing from 5 wt.% to 15 wt.%, the promotion effect of Nb<sub>2</sub>O<sub>5</sub> on activity is observed over all Nb containing catalysts with dramatically increased NO<sub>x</sub> conversions and broadened operation temperature windows. However, further increasing the Nb<sub>2</sub>O<sub>5</sub> loading to 20 wt.% would slightly shrink the operation window and cause N<sub>2</sub> selectivity to decline. Among the catalysts investigated, Nb15CZ exhibits the best NH<sub>3</sub>-SCR activity with an operation window between 190 and 460 °C, which is better than the conventional V<sub>2</sub>O<sub>5</sub>/WO<sub>3</sub>-TiO<sub>2</sub> catalyst (250–400 °C as shown in Fig. 1e). Considerable yields of N<sub>2</sub>O and NO<sub>2</sub> which are observed on CZ are significantly suppressed over Nb containing samples, indicating that Nb<sub>2</sub>O<sub>5</sub> could also enhance the N<sub>2</sub> selectivity, in accord with our previous study [26]. It is clear that the Nb<sub>2</sub>O<sub>5</sub> content is a crucial factor to obtain high NO<sub>x</sub> conversion and N<sub>2</sub> selectivity.

Water vapor is an important component in exhaust gases of vehicles, and its effect is an important issue in SCR catalysts. Therefore, we also investigated the catalytic performance of all catalysts in humid ambient conditions with 5% H<sub>2</sub>O vapor feeding and the results are shown in Figs. 1c and d. It is seen that water vapor only slightly inhibits the catalytic activity below 300 °C, possibly due to its competitive adsorption with NO/NH<sub>3</sub> on the reaction sites [3,11]. The NO<sub>x</sub> conversions over NbCZ catalysts at 500 °C are largely enhanced from 20% to 50% to nearly 100% in presence of H<sub>2</sub>O. This is usually explained as the inhibition effect of H<sub>2</sub>O on NH<sub>3</sub> oxidation [2,14,15]. Meanwhile, addition of H<sub>2</sub>O increases the N<sub>2</sub> selectivity via inhibition of unselective oxidation of NH<sub>3</sub>, as indicated by the decreased amounts of NO<sub>2</sub> and N<sub>2</sub>O.

The influences of hydrothermal ageing and SO<sub>2</sub> poisoning on Nb15CZ were also evaluated and the results are shown in Fig. 1e. Nb15CZ catalyst shows a superior hydrothermal stability with only a slight loss in low-temperature (<300 °C) activity. On the other hand, its resistance to SO<sub>2</sub> poisoning does not appear to be so strong, with a noticeable deactivation at low temperatures and a decrease in the maximum NO<sub>x</sub> conversion. Nevertheless, the sulfur poisoned Nb15CZ catalyst still presents a comparable catalytic performance to fresh V<sub>2</sub>O<sub>5</sub>/WO<sub>3</sub>-TiO<sub>2</sub> catalyst.

#### 3.1.2. NO oxidation

Fig. 2 shows the evolutions of the outlet NO<sub>2</sub> concentration during the NO oxidation measurements. The oxidation of NO over CZ occurs at about 250 °C, while large-scale generations of NO<sub>2</sub> are observed on Nb containing catalysts at much lower temperatures (150–200 °C). This means that the addition of Nb<sub>2</sub>O<sub>5</sub> to CZ leads to stronger NO oxidation activity at low temperatures, in spite of the decline of NO<sub>2</sub> concentration at the temperatures above 300 °C. It is worth noting that at low temperature (150–200 °C), the NO oxidation abilities of catalysts, in the sequence of CZ < Nb5CZ < Nb20CZ < Nb10CZ < Nb15CZ, correlate well with

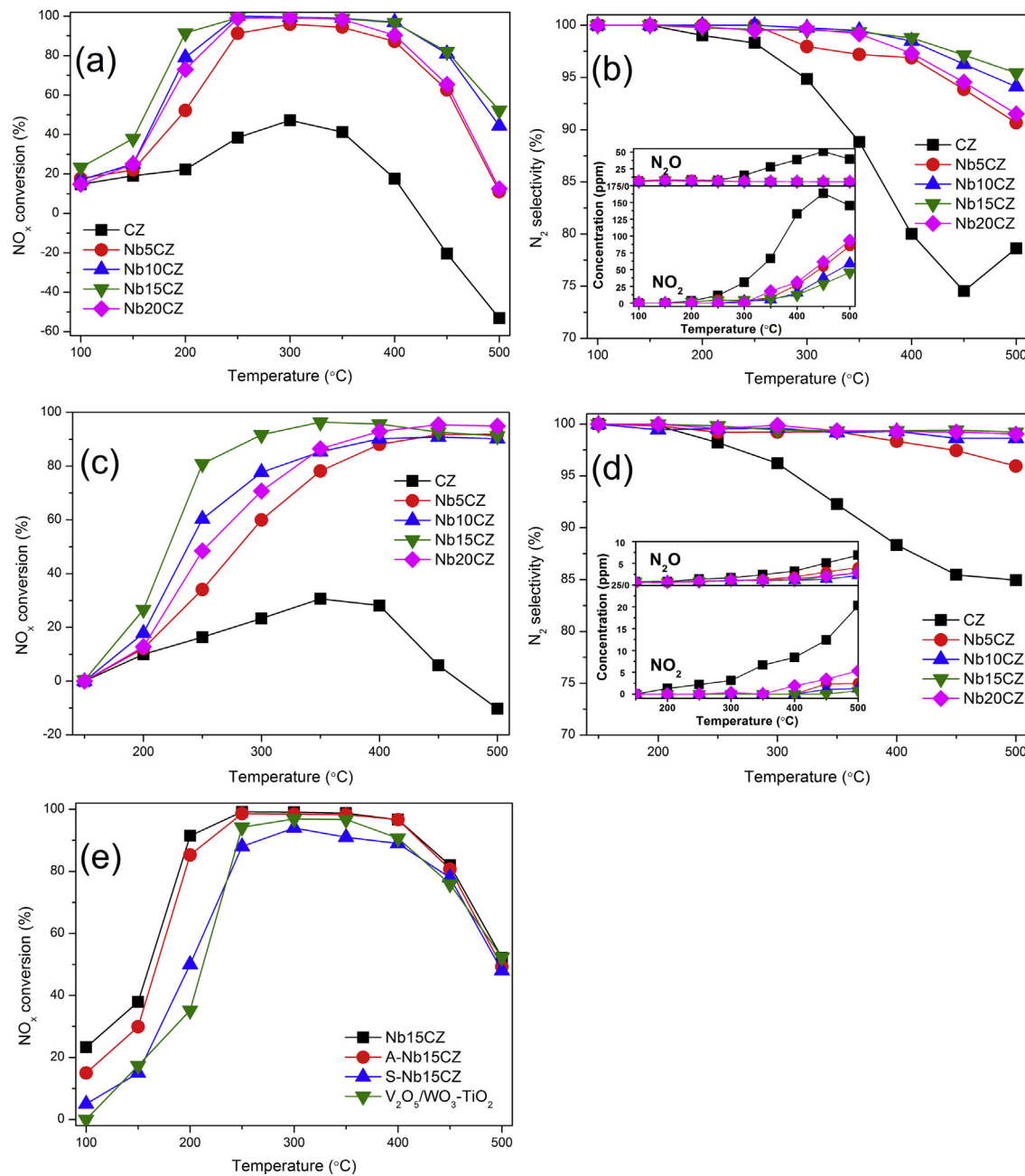


**Fig. 1.**  $\text{NH}_3$ -SCR activities of different catalysts without  $\text{H}_2\text{O}$  (a), (b), (e) and with 5%  $\text{H}_2\text{O}$  (c), (d): (a), (c), (e)  $\text{NO}_x$  conversion, and (b), (d)  $\text{N}_2$  selectivity. Reaction conditions:  $[\text{NH}_3] = [\text{NO}] = 500 \text{ ppm}$ ,  $[\text{O}_2] = 5\%$ ,  $[\text{H}_2\text{O}] = 5\%$ ,  $[\text{CO}_2] = 12\%$ ,  $\text{N}_2$  as balance.  $\text{GHSV} = 3 \times 10^5 \text{ h}^{-1}$ .

their  $\text{NH}_3$ -SCR activities in the same temperature range. The availability of  $\text{NO}_2$  as an important reactant gas is considered as a critical factor to determine the low-temperature activity, as the fast-SCR reaction involving  $\text{NO}_2$  is much faster than the standard SCR [12,35]. Generally, if larger amounts of  $\text{NO}_2$  are generated, higher SCR activities would be attained at low temperatures.

### 3.1.3. $\text{NH}_3$ oxidation

The  $\text{NH}_3$  oxidation experiments were carried out and the results are shown in Fig. 3. It is found in Fig. 3a that the Nb containing catalysts present higher activities for ammonia oxidation than CZ. These results indicate the promotion effect of  $\text{Nb}_2\text{O}_5$  on ammonia oxidation. Pronounced increases in the  $\text{N}_2$  selectivities over the niobium containing catalysts are observed in Fig. 3b, which is due to the lower  $\text{NO}_x$  ( $\text{NO}_2$ , NO and  $\text{N}_2\text{O}$ ) production during the ammonia

oxidation as shown in Fig. 3c. It is noted that the oxidation of  $\text{NH}_3$  over Nb15CZ catalyst is strongly inhibited in the presence of 5%  $\text{H}_2\text{O}$ , with lower by-product yields and higher  $\text{N}_2$  selectivity. This would leave more  $\text{NH}_3$  available for  $\text{NH}_3$ -SCR reaction, resulting in a greatly enhanced  $\text{NO}_x$  conversion at high temperatures as shown in Fig. 1c.

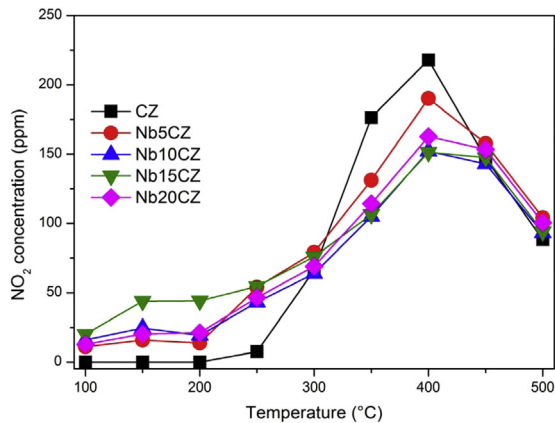
## 3.2. Structural and textural properties

### 3.2.1. XRD and $\text{N}_2$ adsorption

XRD patterns of the catalysts are shown in Fig. S1. All the main reflection patterns of NbCZ catalysts are consistent with the characteristic fluorite-like ceria. No typical patterns of  $\text{Nb}_2\text{O}_5$  crystallites are observed, implying that  $\text{NbO}_x$  species are finely dispersed on the surface of  $\text{Ce}_{0.75}\text{Zr}_{0.25}\text{O}_2$ . Furthermore, the  $\text{CeO}_2$  diffraction peaks

**Table 1**Structural parameters measured by  $N_2$  adsorption and calculated from XRD experiments.

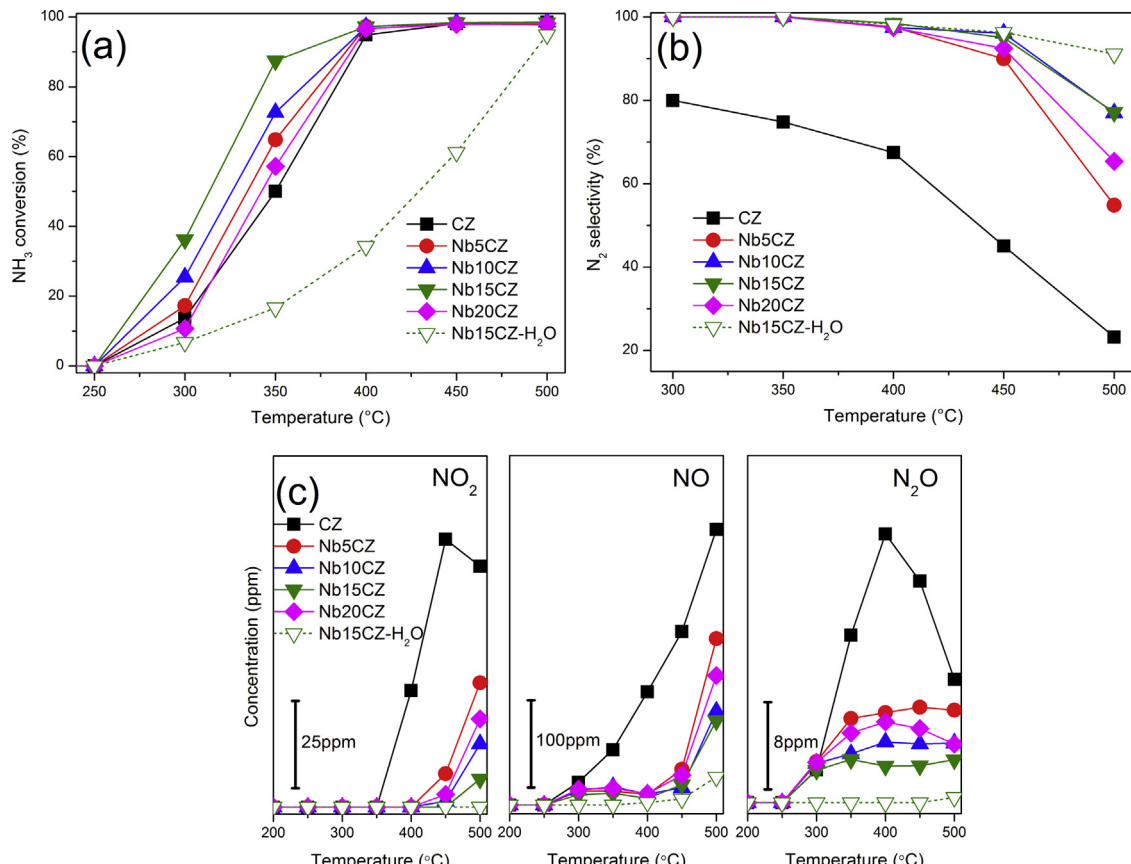
| Sample | $S_{BET}$ ( $m^2 g^{-1}_{cat.}$ ) | Total pore volume ( $cm^3 g^{-1}_{cat.}$ ) | Average pore diameter (nm) | Lattice parameter <sup>a</sup> (Å) | Crystallite size <sup>b</sup> (nm) |
|--------|-----------------------------------|--|----------------------------|------------------------------------|------------------------------------|
| CZ     | 102                               | 0.192                                      | 8.490                      | 5.358                              | 6.8                                |
| Nb5CZ  | 93                                | 0.176                                      | 7.964                      | 5.353                              | 7.1                                |
| Nb10CZ | 85                                | 0.169                                      | 8.360                      | 5.349                              | 7.3                                |
| Nb15CZ | 74                                | 0.162                                      | 8.606                      | 5.347                              | 7.4                                |
| Nb20CZ | 71                                | 0.155                                      | 8.096                      | 5.352                              | 7.4                                |

<sup>a</sup> Calculated from Cohen's method.<sup>b</sup> Calculated from Scherrer's formula.**Fig. 2.** Evolution of  $NO_2$  during  $NO$  oxidation for CZ and NbCZ catalysts. Reaction conditions:  $[NO] = 500$  ppm,  $[O_2] = 5\%$ ,  $N_2$  as balance.  $GHHSV = 3 \times 10^5 h^{-1}$ .

decrease in intensity with increasing the  $Nb_2O_5$  content, indicative of more amorphous structure. The broad diffraction peaks of  $Nb_2O_5$  are assigned to those of bulk niobium oxides. The structural parameters are summarized in Table 1, in which the lattice constant of ceria decreases slightly after  $Nb_2O_5$  loading. It implies that the incorporation of more niobium atoms into the  $CeO_2-ZrO_2$  lattice could result in a contraction of the unit cell due to smaller ionic radius of  $Nb^{5+}$  (0.064 nm) compared to that of  $Ce^{4+}$  (0.087 nm) and  $Zr^{4+}$  (0.072 nm). The decreased  $S_{BET}$  can be ascribed to the blocking effect on pores arising from impregnation of  $NbO_x$  species, which is indicated by the decreased total pore volume as shown in Table 1.

### 3.2.2. Raman

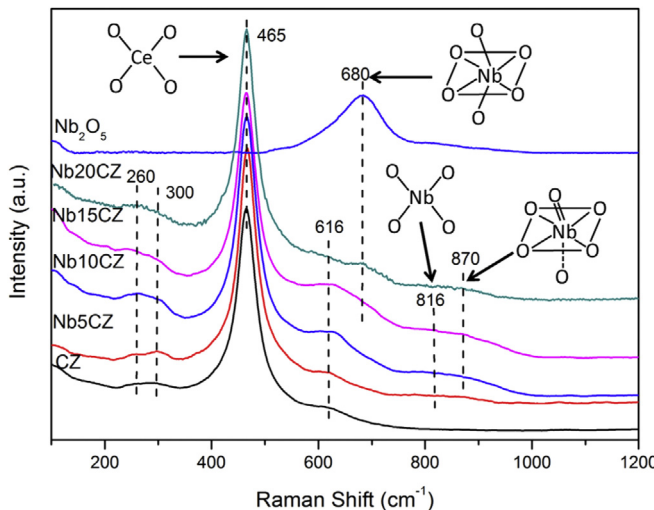
In contrast to the cation-dominated information yielded by XRD, Raman spectra of fluorite-related phases are dominated by lattice oxygen vibrations and are sensitive to crystalline symmetry. As shown in Fig. 4, all the catalysts show typical Raman spectra of  $CeO_2-ZrO_2$  solid solutions with an intense band at  $465\text{ cm}^{-1}$  due to the  $F_{2g}$  Raman active mode of the cubic fluorite structure, which can be viewed as a symmetric breathing mode of oxygen atoms around

**Fig. 3.**  $NH_3$  oxidation activities of CZ and NbCZ catalysts: (a)  $NH_3$  conversion, (b)  $N_2$  selectivity and (c)  $NO_x$  ( $NO_2$ ,  $NO$  and  $N_2O$ ) concentration. Reaction conditions:  $[NH_3] = 500$  ppm,  $[O_2] = 5\%$ ,  $N_2$  as balance.  $GHHSV = 3 \times 10^5 h^{-1}$ .

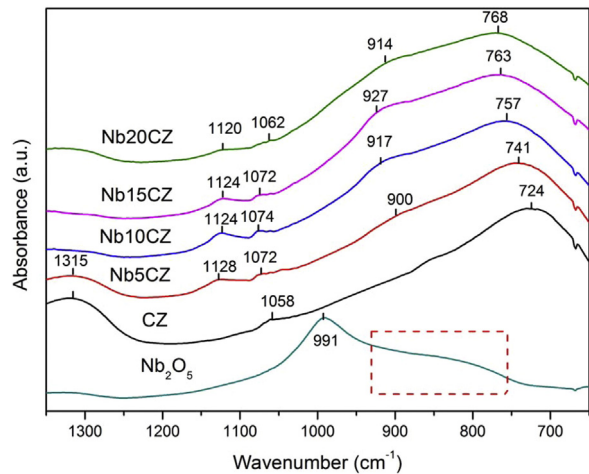
**Table 2**

Absorption edges and band gap widths of different catalysts calculated from UV-vis spectra.

| Sample               | CZ    | Nb <sub>2</sub> O <sub>5</sub> | Nb5CZ | Nb10CZ | Nb15CZ | Nb20CZ | Nb5CZM | Nb15CZM |
|----------------------|-------|--------------------------------|-------|--------|--------|--------|--------|---------|
| Absorption edge (nm) | 471.9 | 404.5                          | 477.1 | 489.7  | 495.3  | 483.9  | 468.4  | 462.2   |
| Band gap width (eV)  | 2.71  | 3.06                           | 2.68  | 2.63   | 2.59   | 2.62   | 2.77   | 2.79    |

**Fig. 4.** Raman spectra of CZ, Nb<sub>2</sub>O<sub>5</sub> and NbCZ catalysts.

cerium ions [25,36,37]. This Raman band depends on several factors including grain size and morphology of CeO<sub>2</sub>–ZrO<sub>2</sub> [36,37]. It has been known in **Table 1** that the crystallite sizes of the samples are around 7 nm, which implies the similarity between crystallite size and grain size within the nanosize range. The full width at half maximum of  $F_{2g}$  Raman band (465 cm<sup>-1</sup>) decreases slightly with the increase of Nb<sub>2</sub>O<sub>5</sub> loading (shown in Fig. S2), which is ascribed to grain growth [38] and correlates with the XRD data. In addition, all NbCZ catalysts show three weak bands at 260, 300 and 616 cm<sup>-1</sup> which are ascribed to the normally Raman inactive transverse and longitudinal optical phonon modes, respectively [25,37]. These bands are due to the relaxation of symmetry rules, which is closely related to the perturbations of ideal fluorite structure caused by displacement of the oxygen atoms from ideal fluorite lattice position [37]. Therefore, the increase in intensity of these bands with Nb<sub>2</sub>O<sub>5</sub> content increasing from 5 wt.% to 15 wt.% is indicative of more oxygen vacancies. Similarly, a further increase to 20 wt. % loading leads to a reduced amount of oxygen vacancies. Bands at 680, 816 and 870 cm<sup>-1</sup> are associated with surface NbO<sub>x</sub> species. According to Ref. [39,40], the broad bands centered at around 816 cm<sup>-1</sup>, which appear initially on the Nb5CZ catalyst, are ascribed to monomeric NbO<sub>x</sub> species with tetrahedral [NbO<sub>4</sub>] structure. This band vanishes when the Nb<sub>2</sub>O<sub>5</sub> loading exceeds 15 wt.%. The band at around 870 cm<sup>-1</sup>, which increases in intensity when increasing the Nb<sub>2</sub>O<sub>5</sub> loading from 10 wt.% to 20 wt.%, is ascribed to highly dispersed polymeric niobium oxide species composed of moderately distorted octahedral [NbO<sub>6</sub>] structures with terminal Nb=O bonds [39,40]. Bands at 680 cm<sup>-1</sup> on high Nb<sub>2</sub>O<sub>5</sub> loading catalysts are assigned to the species with slightly distorted octahedral [NbO<sub>6</sub>] structure connected with sharing corners, particular in form of Nb–O–Nb bond connection [41]. The increase in intensity of bands 680 and 870 cm<sup>-1</sup> at high Nb<sub>2</sub>O<sub>5</sub> loading indicates an increase in degree of polymerization of surface dehydrated NbO<sub>x</sub> species and an increased ratio of polymeric to monomeric NbO<sub>x</sub> species. The bulk Nb<sub>2</sub>O<sub>5</sub> is composed of octahedrally coordinated niobium oxides, only presenting the vibration of Nb–O–Nb bond.

**Fig. 5.** IR spectra of CZ, Nb<sub>2</sub>O<sub>5</sub> and NbCZ catalysts.

### 3.2.3. *ex-situ* IR

The IR spectra of CZ and Nb containing catalysts are shown in **Fig. 5**. The band at 991 cm<sup>-1</sup> and a very broad band at 750–920 cm<sup>-1</sup>, as shown in the inset figure, are attributed to characteristic vibrations of bulk Nb<sub>2</sub>O<sub>5</sub> [41–43]. A typical band centered at 1315 cm<sup>-1</sup> and weak bands at 1058–1062 on CZ are ascribed to the adsorbed carbonate species due to the chemisorption of CO<sub>2</sub> [44,45]. The impregnation of NbO<sub>x</sub> on CZ inhibits the formation of carbonates, indicating that acidic NbO<sub>x</sub> polymerized species could decrease the amount of basic sites on CZ. Bands at 724 cm<sup>-1</sup> correspond to the stretching modes of Ce(Zr)–O–Ce bands [44,45], which shift to higher wavenumbers with increasing Nb<sub>2</sub>O<sub>5</sub> loading. This may result from an overlapping effect by vibration bands of octahedral niobium oxides which locate at higher wavenumbers (750–900 cm<sup>-1</sup>). Bands at 900–927 cm<sup>-1</sup> are attributed to the stretching modes of short Nb=O bonds in surface NbO<sub>x</sub> species, in accordance with the position in NbO<sub>x</sub>/Al<sub>2</sub>O<sub>3</sub>, NbO<sub>x</sub>/ZrO<sub>2</sub> and NbO<sub>x</sub>/TiO<sub>2</sub> catalysts [41]. This Nb=O bond may be in form of either O=Nb–O–Nb in octahedrally polymerized NbO<sub>x</sub> species or O=Nb strongly bonded to CZ. Bands at 1120–1128 cm<sup>-1</sup> which are not observed on CZ, are probably due to combination modes of Nb–O–Nb stretching vibration [41–43]. It is noted that bands ascribed to Nb=O short bonds shift to higher wavenumbers with increasing Nb<sub>2</sub>O<sub>5</sub> loading from 5 wt.% to 15 wt.%, indicative of a decreased bond distance of Nb=O bond. The further increase of Nb<sub>2</sub>O<sub>5</sub> loading to 20 wt.% inversely leads to a slight elongation of Nb=O bond.

### 3.2.4. UV-vis

Fig. S2 shows the UV–vis spectra of the catalysts. For the sake of analysis, the adsorption edges and band gap widths were calculated based on the UV–vis spectra and the results are listed in **Table 2**. For reference, the Nb5CZM and Nb15CZM with 5 wt. % and 15 wt. % Nb<sub>2</sub>O<sub>5</sub> were prepared by mixing the Ce<sub>0.75</sub>Zr<sub>0.25</sub>O<sub>2</sub> and Nb<sub>2</sub>O<sub>5</sub> powders mechanically. As shown in Fig. S2 and **Table 2**, the UV–vis spectra of CZ and Nb<sub>2</sub>O<sub>5</sub> were characterized by a strong absorption in the UV range due to the inter band transition, allowing the estimation of the band gap width to be 2.71 and 3.06 eV and absorption edges to be near 405 and 471 nm, respectively. All Nb

containing catalysts present an absorption edge corresponding to the  $O_{2p}$ – $Ce_{4f}$  ligand-metal charge transfer [46] in the visible range (477–495 nm), which shift to higher wavelengths compared with CZ. This feature is not observed on the mechanically mixed Nb5CZM and Nb15CZM, of which the absorption edges are just composed of two separate absorption thresholds of CZ and  $Nb_2O_5$ . Besides, the band gap widths are also in the same case. These results suggest that the electronic interaction exists between Ce and Nb in NbCZ catalysts and varies with  $Nb_2O_5$  loading. It is known that the presence of  $Ce^{3+}$  ions in the ceria lattice gives rise to an absorption band near 650 nm [13,31], and therefore the partial reduction of  $Ce^{4+}$  to  $Ce^{3+}$  might increase the  $Ce^{3+}/Ce$  ratio and induce the red shift of the absorption edge. In this sense, it is plausible to ascribe the decrease of band gap width and the red shift of the absorption edge in NbCZ catalysts to the increased formation of  $Ce^{3+}$  ions.

### 3.2.5. XPS

To get a better understanding of the chemical state of different elements on the catalyst surface, the selected CZ and Nb15CZ catalysts were investigated by XPS technique. The atomic surface concentrations of different elements are summarized in Table S1, and XPS spectra of Ce 3d, O 1s and Nb 3d are shown in Figs. 6a–c.

The Ce 3d peaks were fitted by searching for the optimum combination of Gaussian bands with the correlation coefficients ( $r^2$ ) above 0.99. The percentages of  $Ce^{3+}$  in Ce on the surface of catalysts were calculated by the method in Ref. [20,47]. Consequently,

the calculated atomic ratio of  $Ce^{3+}/(Ce^{3+}+Ce^{4+})$  is 18% and 39% of CZ and Nb15CZ, respectively. The value of Nb15CZ is much larger than that of CZ. The primary peak at 529.3–530.0 eV ( $O_\beta$ ) is assigned to be lattice oxygen  $O^{2-}$  in metal oxides, and the additional shoulder peak at 531.4–531.8 eV denoted as ( $O_\alpha$ ) is ascribed to chemisorbed oxygen and weakly bonded oxygen species, such as  $O_2^{2-}$  and  $O^-$  belonging to defect-oxides or hydroxyl-like groups [19,48]. The relative ratio of  $O_\alpha/(O_\alpha+O_\beta)$  is quantified based on the area of  $O_\beta$  and  $O_\alpha$  peaks, which are 17% and 9% on Nb15CZ and CZ, respectively. This value obviously increases on the Nb15CZ sample accompanied with the same trend of the  $Ce^{3+}/(Ce^{3+}+Ce^{4+})$  ratio shown above. The increased amount of surface oxygen can be directly attributed to the formation of more  $Ce^{3+}$  on Nb15CZ, as oxygen vacancies and active oxygen are associated with a reduction of two neighboring  $Ce^{4+}$  to  $Ce^{3+}$  in the cubic fluorite [18]. According to the Handbook of X-ray Photoelectron Spectroscopy, the two peaks at 206.8 eV and 209.6 eV representing  $Nb\ 3d_{5/2}$  and  $Nb\ 3d_{3/2}$  with a spin-orbit splitting of 2.6 eV should be attributed to the  $Nb^{5+}$  species [48], implying that the main structure of  $NbO_x$  oxides species in N15CZ should be octahedral  $NbO_6$  [39]. These results are consistent with Raman results.

### 3.3. Redox properties

#### 3.3.1. $H_2$ -TPR

Fig. 7 shows the  $H_2$ -TPR profiles of NbCZ and pure CZ to estimate the reducibility of different catalysts. The  $H_2$  consumption of

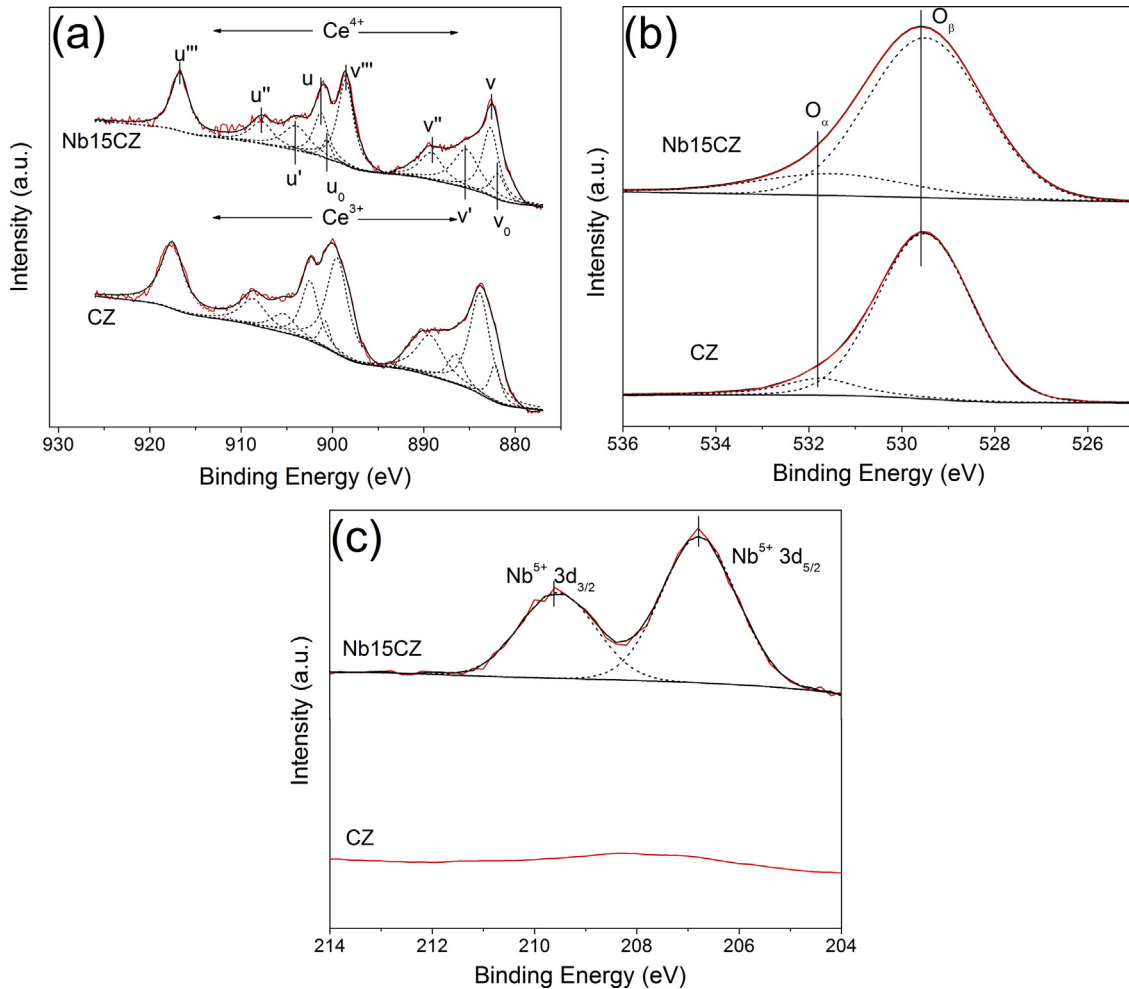
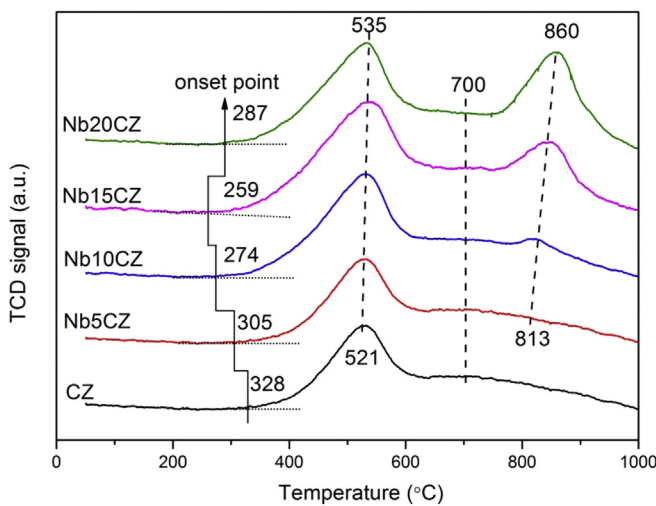
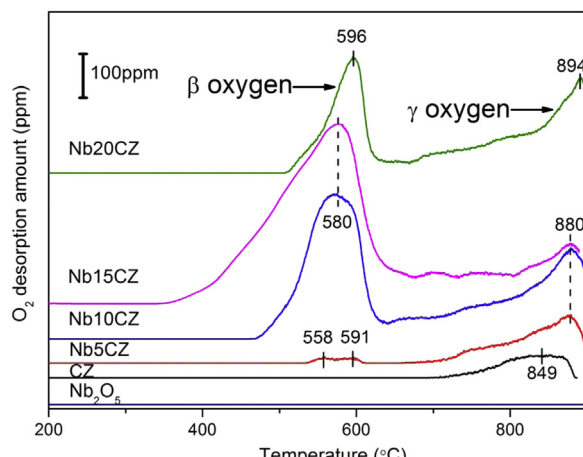


Fig. 6. XPS spectra of CZ and Nb15CZ catalysts: (a) Ce 3d, (b) O 1s and (c) Nb 3d.

Fig. 7.  $\text{H}_2$ -TPR profiles of CZ and NbCZ catalysts.

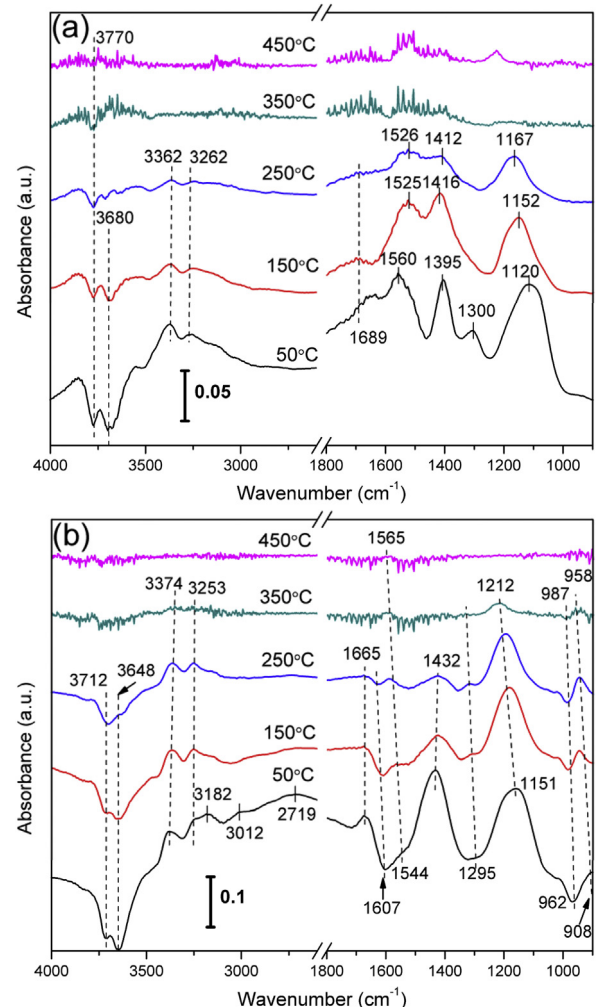
different reduction peaks was calculated by dividing up and fitting the curves and the results are summarized in Table S2. As shown in Fig. 7, there is a distinct reduction peak at 400–600 °C with the maximum at 521–535 °C and a broad reduction peak at 600–800 °C, centered at 700 °C, for CZ. The low-temperature peak is attributed to the reduction of active oxygen from ceria promoted by Zr doping and/or Nb modification [8,28]. The high-temperature peak corresponds to the reduction of lattice oxygen from unpromoted ceria, i.e., non-active lattice oxygen [12,13]. The additional peak at 813–860 °C for the Nb containing samples results from the reduction of surface  $\text{NbO}_x$  species, i.e., the capping oxygen from  $\text{NbO}_x$  [49,50]. Clearly, the loading of  $\text{Nb}_2\text{O}_5$  modifies the redox properties of CZ. Although there is a trend that the peak temperature shifts slightly towards higher temperature with increasing the  $\text{Nb}_2\text{O}_5$  loading, it does not mean that the reducibility of NbCZ catalysts is suppressed by niobia loading. Instead, the onset reduction temperature of active oxygen is significantly lowered from 328 to 259 °C, indicating the occurrence of more facile reduction at lower temperatures. The sequence of the onset reduction temperature is  $\text{Nb15CZ} < \text{Nb10CZ} < \text{Nb20CZ} < \text{Nb5CZ} < \text{CZ}$ . Furthermore, the amount of surface active oxygen species is much larger on NbCZ catalysts, especially when considering their smaller surface area compared with CZ. The order of the amount of surface active oxygen species turns to be  $\text{Nb15CZ} > \text{Nb10CZ} > \text{Nb20CZ} > \text{Nb5CZ} > \text{CZ}$ . This trend as well as that

Fig. 8.  $\text{O}_2$ -TPD curves of CZ,  $\text{Nb}_2\text{O}_5$  and NbCZ catalysts.

of onset reduction temperature correlates well with the NO and  $\text{NH}_3$  oxidation activities as shown in Fig. 2 and Fig. 3, and suggests that some strong interaction occurs between  $\text{Nb}^{n+}$  and  $\text{Ce}^{n+}$  at the  $\text{Nb}^{n+}-\text{O}-\text{Ce}^{n+}$  ( $\text{Zr}^{n+}$ ) interface. The increase in  $\text{H}_2$  consumption at 813–860 °C is due to the reduction of excessive polymerized surface  $\text{NbO}_x$  species which may lead to the formation of bulk niobia [50].

### 3.3.2. $\text{O}_2$ -TPD

$\text{O}_2$ -TPD measurements were performed and the results are shown in Fig. 8 and Table S3. As shown in Fig. 8, there is almost no  $\text{O}_2$  release detected on  $\text{Nb}_2\text{O}_5$  during the whole desorption process, indicative of a poor oxygen mobility of  $\text{Nb}_2\text{O}_5$ . Only a weak  $\text{O}_2$  desorption peak ( $\gamma$ ) centered at 849 °C is observed on CZ. As for Nb-containing catalysts, apart from the high-temperature desorption peak ( $\gamma$ ) around 880 °C, a distinct  $\text{O}_2$  desorption peak ( $\beta$ ) appears in the temperature range of 300–650 °C. The  $\beta$  and  $\gamma$  desorption peak are assigned to  $\text{O}_2$  stripped from surface active oxygen sites ( $\text{O}_2^-$ ,  $\text{O}^-$ ) and lattice oxygen sites ( $\text{O}_2^{2-}$ ), respectively [33,51]. The onset temperature and desorption amount of  $\beta$  peak follow a sequence of  $\text{Nb15CZ} < \text{Nb10CZ} < \text{Nb20CZ} < \text{Nb5CZ} < \text{CZ}$  and  $\text{Nb15CZ} > \text{Nb10CZ} > \text{Nb20CZ} > \text{Nb5CZ} > \text{CZ}$ , respectively. It suggests that the availability of active oxygen depends to a great extent on the  $\text{Nb}_2\text{O}_5$  loading amount. Therefore, it is reasonable to ascribe the increase in the amount of active oxygen species ( $\text{O}_2^-$ ,  $\text{O}^-$ ) to the

Fig. 9. DRIFT spectra of (a) CZ and (b) Nb15CZ pretreated in 1000 ppm  $\text{NH}_3/\text{N}_2$  at room temperature for 1 h and then purged by  $\text{N}_2$  from 50 to 450 °C at a heating rate of  $10\text{ }^\circ\text{C min}^{-1}$ .

interaction between  $\text{Ce}^{n+}$  and  $\text{Nb}^{n+}$ . The amount of available lattice oxygen ( $\gamma$ ) over NbCZ catalysts also increases remarkably compared with CZ, indicating that lattice oxygen mobility is improved after  $\text{Nb}_2\text{O}_5$  loading. An additional small desorption peak ( $\alpha$ ) at 136 °C (not shown) is observed only on the Nb15CZ sample, which is assigned to the desorption of physically adsorbed oxygen species ( $\text{O}_2$ ) [33,51].

### 3.4. Acidity

#### 3.4.1. IR spectra of $\text{NH}_3$ adsorption

Figs. 9a–b show the DRIFT spectra of  $\text{NH}_3$  derived species over CZ and Nb15CZ catalysts arising from contact of  $\text{NH}_3$  at different temperatures in the region 4000–2600 and 1800–900  $\text{cm}^{-1}$ . More Lewis acid sites than Brønsted acid sites are present on the CZ catalyst. This is indicated by the higher intensities of  $\text{NH}_3$  species (3362, 3262 and 1120–1167  $\text{cm}^{-1}$ ) and  $\text{NH}_2$  species (1526–1560  $\text{cm}^{-1}$  and 1300  $\text{cm}^{-1}$ ) both coordinated to Lewis acid sites, compared to the intensities of  $\text{NH}_4^+$  (1395–1412  $\text{cm}^{-1}$ ) species bound to Brønsted acid sites [9–12,14,52]. The negative bands at 3770 and 3680  $\text{cm}^{-1}$  are assigned to the consumption of hydroxyl groups by  $\text{NH}_3$  to form  $\text{NH}_4^+$  [14], which regain the initial level due to  $\text{NH}_4^+$  desorption with the temperature increase. In addition, amide ( $\text{NH}_2$ ) species are derived from the dehydrogenation of ammonia on Lewis acid sites via partial oxidation by active oxygen [13,14].

Some new bands are observed on the Nb15CZ catalyst. Compared with CZ, Nb15CZ possesses much more Lewis and Brønsted acid sites despite its smaller surface area, suggesting that the catalyst surface acidity is significantly enhanced by  $\text{Nb}_2\text{O}_5$  loading. When the temperature rises up to 350 °C, the adsorbed  $\text{NH}_3$  species on Lewis acid sites (1151–1212  $\text{cm}^{-1}$ ) are more thermally stable than those on Brønsted acid sites (1665 and 1432  $\text{cm}^{-1}$ ) [9,12–14,52]. The negative band at 962–987  $\text{cm}^{-1}$  is due to the consumption of the  $\text{Nb}=\text{O}$  terminal bond by  $\text{NH}_3$  adsorption [25,41]. The simultaneous disappearance of bands at 1151–1212 and 962–987  $\text{cm}^{-1}$  with the increase in temperature indicates that the stable Lewis acid sites are closely related to the  $\text{Nb}=\text{O}$  bonds in  $\text{NbO}_x$  species. It is worth noting that the adsorbed  $\text{H}_2\text{O}$  on the surface of NbCZ shows an obvious consumption as indicated by the negative bands at 1607  $\text{cm}^{-1}$  [14], indicating that much more  $\text{H}_2\text{O}$  is consumed on Nb15CZ than on CZ during  $\text{NH}_3$  adsorption. These negative bands and the bands of  $\text{NH}_4^+$  species bound to Brønsted acid sites (1665 and 1432  $\text{cm}^{-1}$ ) vanish simultaneously, suggesting that the adsorbed  $\text{H}_2\text{O}$  reacts readily with the adjacent  $\text{Nb}=\text{O}$  bond to form  $\text{Nb}=\text{OH}$  as Brønsted acid site. It cannot be ignored that bands ascribed to  $\text{NH}_2$  species (1544–1565  $\text{cm}^{-1}$  and 1295  $\text{cm}^{-1}$ ) at high temperature (>250 °C), are more notable on Nb15CZ than those on CZ, indicating the presence of more  $\text{NH}_2$  species, which may promote the SCR reaction at high temperature as  $\text{NH}_2$  is a very important intermediate of the E–R reaction route [13,52].

#### 3.4.2. $\text{NH}_3$ -TPD

$\text{NH}_3$ -TPD was performed to estimate the surface acidities of CZ and NbCZ catalysts and the profiles are shown in Fig S3. These profiles can be divided into three different overlapping peaks, which could be ascribed to the desorbed ammonia species with different thermal stability. Combined with the analysis of FTIR results, different categories of acid sites are listed in Table 3. Clearly, increases in total amount and strength of acid sites are observed upon addition of  $\text{Nb}_2\text{O}_5$ , suggesting that the  $\text{Nb}_2\text{O}_5$  loading increases the catalyst surface acidity. The weak Lewis acid sites ( $L_1$ ) of CZ are derived from coordinatively unsaturated  $\text{Ce}^{n+}$  or  $\text{Zr}^{n+}$  sites [19,53], while the Brønsted acid sites ( $B$ ) are associated with surface hydroxyl groups [13,19]. For NbCZ catalysts, the increased amount of Brønsted ( $B$ )

and strong Lewis ( $L_2$ ) acid sites is due to the introduction of  $\text{NbO}_x$  species.

### 3.5 In-situ DRIFTS study

#### 3.5.1. $\text{NO} + \text{O}_2$ co-adsorption

Fig. 10a presents the *in-situ* DRIFTS spectra of  $\text{N}_x\text{O}_y$  adsorption on CZ at various temperatures. Several bands in the region of 1000–1605  $\text{cm}^{-1}$  are detected. The intensities of bands at 1437, 1301 and 1185  $\text{cm}^{-1}$  decrease with temperature increasing and finally vanish at 250 °C, which is accompanied by the increase of the bands at 1533–1605, 1224 and 1005–1025  $\text{cm}^{-1}$ . This is due to the transformation of monodentate (1437  $\text{cm}^{-1}$ ), bidentate nitrito (1301  $\text{cm}^{-1}$ ) and nitrosyl anion (1185  $\text{cm}^{-1}$ ) species at  $\text{Ce}^{n+}$  sites to more thermally stable monodentate (1533 and 1005  $\text{cm}^{-1}$ ), bidentate (1560 and 1025  $\text{cm}^{-1}$ ) and bridging (1605, 1582 and 1224  $\text{cm}^{-1}$ ) nitrates [12,21,23,54,55]. All these results indicate that the  $\text{NO}_3^-$  species are formed due to the oxidation of adsorbed  $\text{NO}^-$  and  $\text{NO}_2^{2-}$  species by surface oxygen species promoted by increasing temperature [54]. At temperatures higher

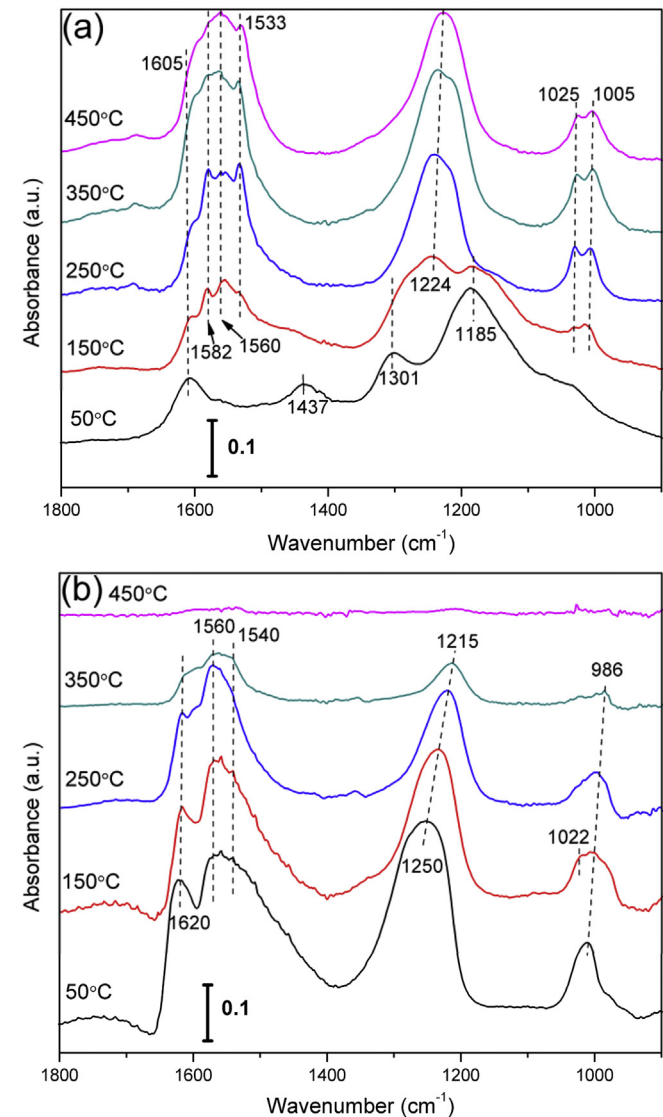


Fig. 10. DRIFT spectra of (a) CZ and (b) Nb15CZ in 1000 ppm  $\text{NO} + 10\%$   $\text{O}_2$  from 50 to 450 °C at a heating rate of 10 °C  $\text{min}^{-1}$ .

**Table 3**The surface acidity calculated from  $\text{NH}_3$  desorption amount in  $\text{NH}_3$ -TPD.

| Sample | Acidity <sup>a</sup> ( $\mu\text{mol m}^{-2}$ cat.) | Low temperature       |                                      | High temperature                   |      | $T$ (°C) | $L_2$ ( $\mu\text{mol m}^{-2}$ cat.) |
|--------|---|-----------------------|--------------------------------------|------------------------------------|------|----------|--------------------------------------|
|        |   | $T$ (°C) <sup>b</sup> | $L_1$ ( $\mu\text{mol m}^{-2}$ cat.) | $B$ ( $\mu\text{mol m}^{-2}$ cat.) |      |          |                                      |
| CZ     | 1.32  | 152                   | 1.20                                 | 227                                | 0.12 | –        | –                                    |
| Nb5CZ  | 2.66  | 166                   | 2.14                                 | 270                                | 0.31 | 306      | 0.21                                 |
| Nb10CZ | 3.57  | 176                   | 2.49                                 | 270                                | 0.80 | 310      | 0.28                                 |
| Nb15CZ | 4.65  | 173                   | 3.36                                 | 267                                | 0.99 | 316      | 0.31                                 |
| Nb20CZ | 2.63  | 161                   | 2.09                                 | 240                                | 0.28 | 315      | 0.26                                 |

<sup>a</sup> Calculated from the specific  $\text{NH}_3$  desorption amount per  $S_{\text{BET}}$  of the catalysts.<sup>b</sup> Central desorption temperature of the ammonia bound to different acid sites.

than 250 °C, the surface nitrates could be stably stored on the CZ surface.

Fig. 10b shows the *in-situ* DRIFTS spectra of  $\text{N}_x\text{O}_y$  adsorption on Nb15CZ. Compared with CZ, all bands decrease in intensity more rapidly with temperature, indicating that the thermal stability of nitrates on CZ is greatly weakened by  $\text{Nb}_2\text{O}_5$  loading. The overlapping band centered at 1215–1250  $\text{cm}^{-1}$  could be divided into two bands at 1250–1290 and 1208–1250  $\text{cm}^{-1}$ , which are assigned to monodentate nitrates and bridging nitrates, respectively [12,20,21,23]. The weak band at 1560  $\text{cm}^{-1}$  was due to bidentate nitrates [12,21,55]. The band at 1620  $\text{cm}^{-1}$  could be attributed to adsorbed  $\text{NO}_2$  in the literatures [15,23,55]. However, considering that the variation of this band is similar to that at 1250  $\text{cm}^{-1}$ , it is more reasonably attributed to bridging nitrates [12,20,55]. Compared with CZ, adsorbed  $\text{NO}_3^-$  species are formed at much lower temperatures on Nb15CZ, which should be attributed to the participation of more active surface oxygen in the oxidation of adsorbed  $\text{NO}^-$  and  $\text{NO}_2^{2-}$  species.

### 3.5.2. $\text{NO} + \text{NH}_3 + \text{O}_2$ reaction

To identify the surface adsorbed species on the catalysts under reaction conditions, DRIFT spectra were recorded from 150 to 450 °C in a flow of  $\text{NO} + \text{NH}_3 + \text{O}_2$ . Various species, such as  $\text{NO}^-$  species (1180  $\text{cm}^{-1}$ ), nitrito species (1398 and 1292  $\text{cm}^{-1}$ ), nitrates (1602, 1576, 1550, 1533, 1234, 1212, 1026 and 1008  $\text{cm}^{-1}$ ),  $\text{NH}_4^+$  species on Brønsted acid sites (1688  $\text{cm}^{-1}$ ) and  $\text{NH}_3$  coordinated to Lewis acid sites (3385 and 3280  $\text{cm}^{-1}$ ), are observed on CZ in Fig. 11a. Raising the temperature results in a decrease in intensities of the bands assigned to  $\text{NO}^-$ , nitrito and  $\text{NH}_3$  ad-species. On the contrary, the intensities of nitrate species are strengthened, suggesting that the catalyst surface is strongly covered by nitrates. Intensities of nitrate bands at various temperatures are similar to those attained upon  $\text{N}_x\text{O}_y$  adsorption (Fig. 10a), which implies that it is difficult for ammonia to be adsorbed on CZ due to the dominating surface coverage by nitrates.

Fig. 11b shows the DRIFT spectra in a flow of  $\text{NO} + \text{NH}_3 + \text{O}_2$  on Nb15CZ. It can be concluded that there are mainly  $\text{NH}_3$  (3211  $\text{cm}^{-1}$ ),  $\text{NH}_4^+$  (1681  $\text{cm}^{-1}$ ) and nitrates (1532–1606, 1208–1231 and 1004  $\text{cm}^{-1}$ ) present on the catalyst. Intensities of bands ascribed to adsorbed  $\text{NH}_3/\text{NH}_4^+$  and nitrate species are greatly weakened compared with those attained in the  $\text{NH}_3$  adsorption (Fig. 9b) and  $\text{N}_x\text{O}_y$  adsorption (Fig. 10b), indicating that the adsorbed ammonia and nitrates are very active in the SCR reaction on this catalyst. The negative bands at 948 and 3737  $\text{cm}^{-1}$  indicate that the enhanced Brønsted acidity could result from surface hydroxyl groups and  $\text{Nb}=\text{O}$  bonds [25,53], which further promotes the adsorption of ammonia. New bands appear at 1356 and 1382  $\text{cm}^{-1}$ , which may be assigned to the intermediate species from the combination of surface adsorbed  $\text{NH}_3$  and  $\text{N}_x\text{O}_y$  species, e.g.,  $\text{NH}_4\text{NO}_3$  (1380  $\text{cm}^{-1}$ ) in agreement with Ref. [56].

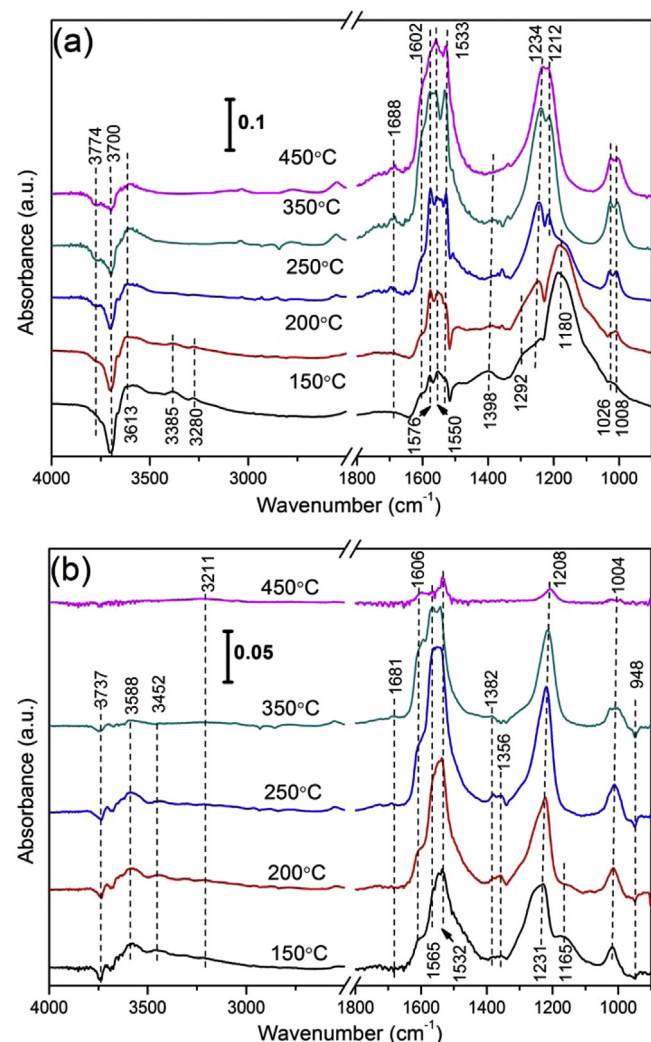


Fig. 11. DRIFT spectra of (a) CZ and (b) Nb15CZ in 1000 ppm NO + 1000 ppm  $\text{NH}_3 + 10\%$   $\text{O}_2$  from 150 to 450 °C.

## 4. Discussion

### 4.1. Catalyst structure and surface acidity

Analysis of the structure of the supported Nb phase by XRD and Raman shows no evidence of  $\text{Nb}_2\text{O}_5$ , which suggest Nb phase is present as a surface species. According to the structural information contained in the Raman and IR spectra,  $\text{NbO}_x$  species with tetrahedral  $[\text{NbO}_4]$  structure appear initially at low  $\text{Nb}_2\text{O}_5$  loading, as the  $[\text{NbO}_4]$  structure displays monomeric characteristics with only 4-coordinations to surrounding oxygen. With  $\text{Nb}_2\text{O}_5$  loading increasing, polymeric  $\text{NbO}_x$  species with octahedral  $[\text{NbO}_6]$  struc-

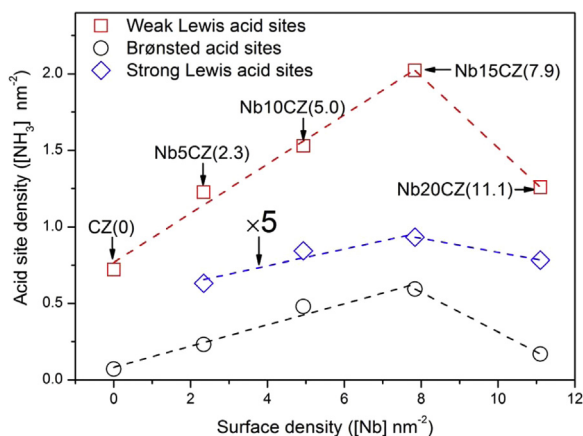


Fig. 12. Correlations between acid site density and surface Nb density on NbCZ catalysts.

ture are gradually formed and become dominant by connecting isolated  $[\text{NbO}_4]$  units with bridging oxygen. When the  $\text{Nb}_2\text{O}_5$  loading exceeds the monolayer coverage amount, multi-layer  $\text{NbO}_x$  and even bulk niobia may be formed. Note that such a proposed structure evolution is evidenced by the Raman and  $\text{H}_2$ -TPR results, and is also consistent with the previous studies [41,53]. Fig. 12 shows the correlation between the densities of different categories of acid sites and surface Nb density. Both Brønsted acidity and strong Lewis acidity increase in a quasi-linear manner with the surface Nb density until peaking at  $7.9 \text{ [Nb] nm}^{-2}$ , and then drop dramatically at higher  $\text{Nb}_2\text{O}_5$  loadings. Based on the results of *in-situ* FTIR of ammonia adsorption, these acid sites are closely associated with the  $\text{Nb}=\text{O}$  and  $\text{Nb}–\text{O}–\text{Nb}$  bonds in  $\text{NbO}_x$  species, and in dynamic conditions, they can be transformed into each other ( $\text{Nb}–\text{OH} + \text{OH} \leftrightarrow \text{Nb}=\text{O} + \text{H}_2\text{O}$ ). This relationship between acidity and  $\text{Nb}_2\text{O}_5$  loading amount confirms the previous studies that abundance of Brønsted acid sites is closely related to extensive polymeric  $\text{NbO}_x$  species, which increases with  $\text{Nb}_2\text{O}_5$  loading amount until dispersion capacity, and with further  $\text{Nb}_2\text{O}_5$  loading decreases due to the formation of multi-layer  $\text{NbO}_x$  species [13,53]. Therefore,  $7.9 \text{ [Nb] nm}^{-2}$  is assumed to be approximately the dispersion capacity for formation of  $\text{NbO}_x$  monolayer coverage. It is also notable in Fig. 12 that original weak Lewis acidity of CZ is also

increased by  $\text{Nb}_2\text{O}_5$  loading, which can be attributed to the electron withdrawing of an  $\text{NbO}_x$  species in proximity of  $\text{Ce}^{n+}/\text{Zr}^{n+}$  Lewis acid sites. Similar cases have been widely observed on  $\text{NbO}_x/\text{ZrO}_2$ ,  $\text{SO}_4^{2-}/\text{CeO}_2$ , and  $\text{NiO}–\text{CeO}_2–\text{ZrO}_2–\text{SO}_4^{2-}$  catalysts [19,21,53].

This structure evolution can be easily illustrated with an “incorporation model” presented in Fig. 13, with the basic idea that surface  $\text{NbO}_x$  species are formed by Nb ions piling up along the two-dimensional directions of the monolayer on the surface of  $\text{Ce}_x\text{Zr}_{1-x}\text{O}_2$  ( $x \geq 0.5$ ).  $\text{O}^{2-}$  ions are arranged as cubic close packed in “fluorite-like” CZ, with (111) plane preferentially exposed on CZ and some tetrahedral vacant sites existing in the  $\text{O}^{2-}$  close packed structure [30,57]. As shown in the planar model, one structure unit contains another tetrahedral vacant site besides the one already occupied by  $\text{Ce}^{4+}$  or  $\text{Zr}^{4+}$ . Based on the CZ lattice parameter ( $0.536 \text{ nm}$ ) and  $\text{O}^{2-}$  radius ( $0.140 \text{ nm}$ ), the area of this structure unit is  $0.124 \text{ nm}^2$  and accordingly the vacancy density and the maximum radius of the tetrahedral vacant site are calculated as  $8.06 \text{ [atom] nm}^{-2}$  and  $0.092 \text{ nm}$ , respectively. All these tetrahedral vacant sites can provide enough space for dispersion of  $\text{Nb}^{n+}$  ions due to the smaller radii of  $\text{Nb}^{5+}$  ( $0.064 \text{ nm}$ ), so the theoretical dispersion capacity of  $\text{NbO}_x$  on CZ should be  $8.06 \text{ [Nb] nm}^{-2}$ . It is shown that the surface Nb density over  $\text{Nb}15\text{CZ}$  ( $7.9 \text{ [Nb] nm}^{-2}$ ) is very close to this value, which confirms the assumption proposed above. When  $\text{Nb}^{n+}$  ions are incorporated into the unoccupied vacant sites, the accompanying  $\text{O}^{2-}$  ions would migrate above  $\text{Nb}^{n+}$  ions to maintain electric neutrality. For isolated  $\text{NbO}_x$  species ( $[\text{NbO}_4]$  structure), each incorporated  $\text{Nb}^{4+}$  ion is accompanied by only one  $\text{O}^{2-}$  ion (occupying area:  $0.062 \text{ nm}^2$ ) to maintain electric neutrality, which produce no shielding effect for the vacant site in the neighboring structure unit. However, three capping  $\text{O}^{2-}$  ions (occupying area:  $0.185 \text{ nm}^2$ ) are utilized by one  $\text{Nb}^{5+}$  ion to build  $[\text{NbO}_6]$  structure, thus making the adjacent vacant sites partly or completely shielded and preventing them from being occupied by other niobium ions. With the increasing degree of polymerization of  $\text{NbO}_x$  species, a close-packed monolayer could be formed upon  $\text{Nb}_2\text{O}_5$  reaching its dispersion capacity while only about 2/3 of the surface vacant sites can be utilized and some unoccupied vacancies are still underneath. The further increase of  $\text{Nb}_2\text{O}_5$  loading would induce the excessive  $\text{Nb}^{n+}$  ions to be incorporated into the tetrahedral vacant sites of the close-packed capping oxygen of  $\text{NbO}_x$ , leading to a multi-layer structure. Therefore, it is easy to understand the  $\text{NbO}_x$  species structured with both  $[\text{NbO}_4]$  and  $[\text{NbO}_6]$ .

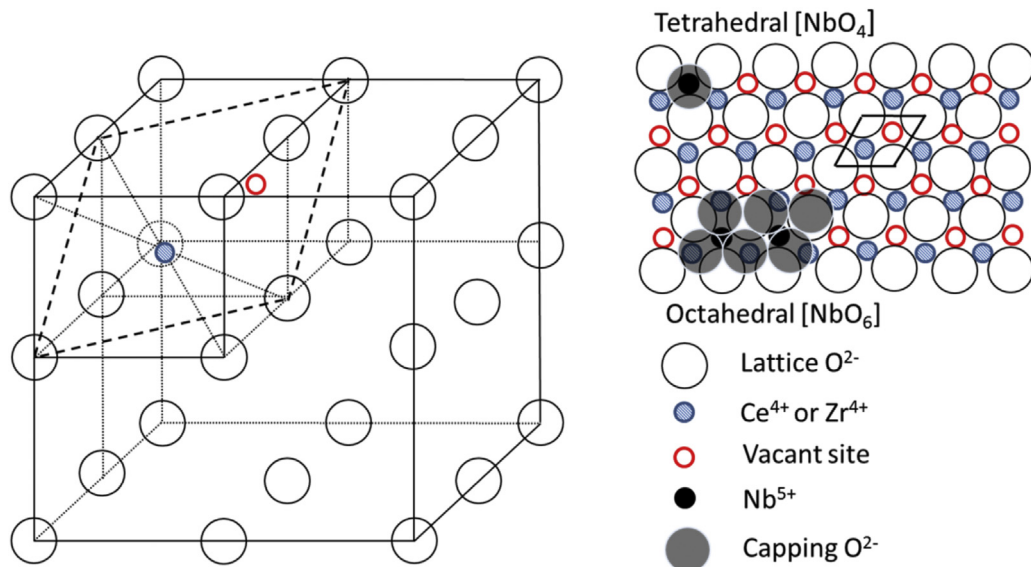
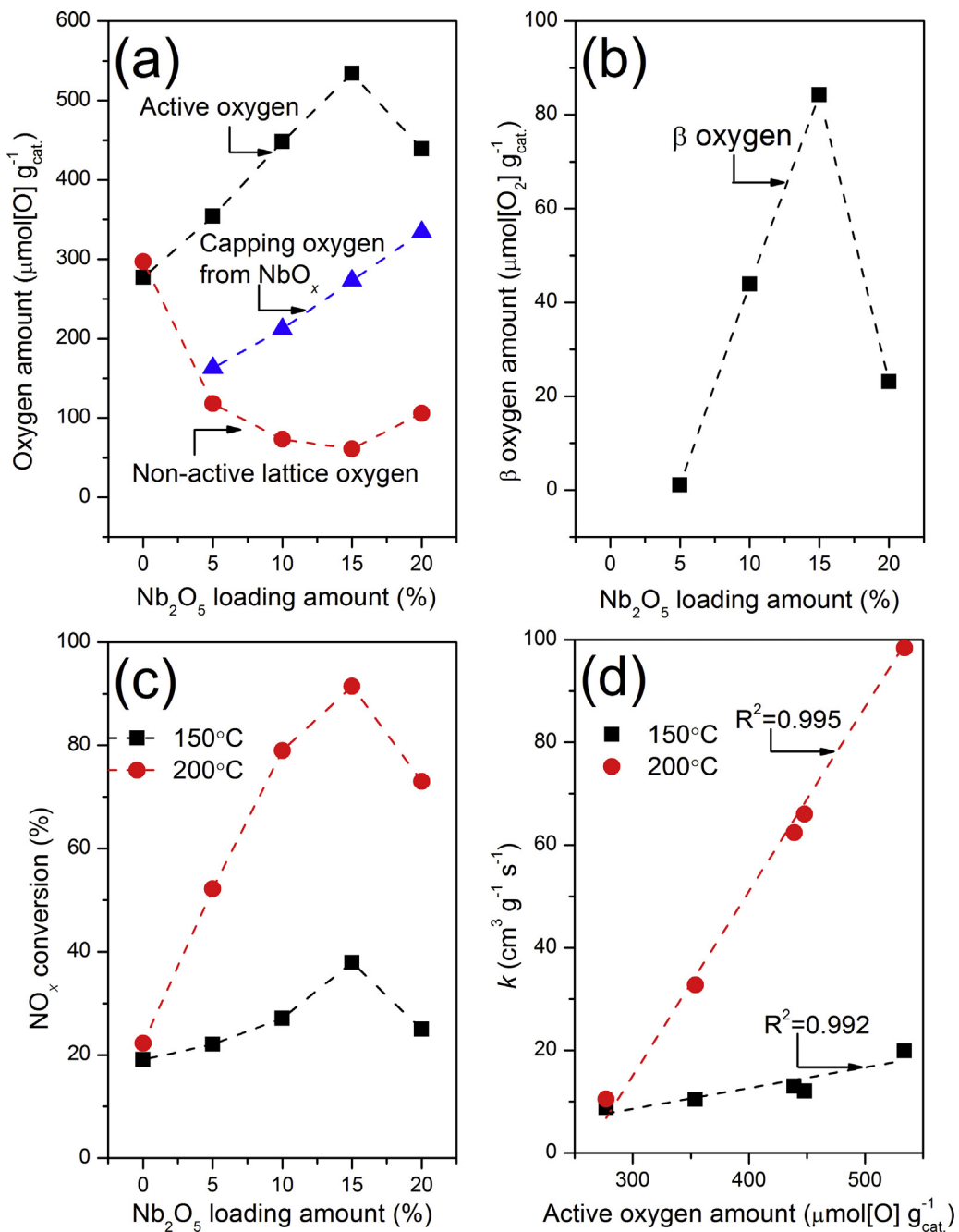


Fig. 13. Planar structure diagram of  $\text{Ce}_x\text{Zr}_{1-x}\text{O}_2$  (111) plane and the tetrahedrally and octahedrally coordinated  $\text{NbO}_x$  species on CZ surface.

units below or near monolayer would make better utilization of surface vacant sites and be 100% dispersed without being covered by upper  $\text{NbO}_x$  layers, thus making  $\text{Nb}=\text{O}$  and  $\text{Nb}–\text{O}–\text{Nb}$  bonds exposed outside as acid sites. This characteristic is clearly indicated by the co-presence of bands at 816 and 870  $\text{cm}^{-1}$  in Raman spectra with  $\text{Nb}_2\text{O}_5$  loading amount varying from 10% to 15%. However, most of Nb ions in multi-layer  $\text{NbO}_x$  or bulk  $\text{Nb}_2\text{O}_5$  are buried deep in the interior, resulting in the low utilization of Nb ions for formation of acid sites. This in theory explains the decreases in Brønsted acidity and strong Lewis acidity with further increasing  $\text{Nb}_2\text{O}_5$  loadings above dispersion capacity. Noticeably, the Nb ions in monomeric and polymeric, rather than in multi-layer  $\text{NbO}_x$  species will have more opportunities to contact the CZ surface.

#### 4.2. Catalyst structure and active sites

Apart from existence in supported  $\text{NbO}_x$  species, some Nb ions would enter into the CZ lattice as the radius of  $\text{Nb}^{5+}$  (0.064 nm) is similar to that of  $\text{Ce}^{4+}$  (0.087 nm) and  $\text{Zr}^{4+}$  (0.072 nm). For NbCZ catalysts, substitution of a  $\text{Ce}^{4+}/\text{Zr}^{4+}$  ion by  $\text{Nb}^{5+}$  in the CZ network brings an excess electron which could be compensated by the formation of a  $\text{Ce}^{3+}$  ion. These  $\text{Ce}^{3+}$  ions are vital to the formation of oxygen vacancies and less bonded oxygen because  $\text{Ce}^{3+}$  could result in charge imbalance and unsaturated chemical bonds [21,28]. In other words, the adjacent oxygen species around cerium sites are activated by Nb. It is known that Ce sites that possess facile  $\text{Ce}^{4+}$  to  $\text{Ce}^{3+}$  redox cycle serve as active sites in ceria based cata-



**Fig. 14.** (a) Amounts of different oxygen species calculated from  $\text{H}_2$ -TPR experiment and (b) amount of  $\beta$  oxygen calculated from  $\text{O}_2$ -TPD experiment as a function of the  $\text{Nb}_2\text{O}_5$  loading amount, (c)  $\text{NO}_x$  conversion as a function of  $\text{Nb}_2\text{O}_5$  loading amount at 150 and 200 °C, and (d) correlations between the amount of active oxygen and pseudo-first order rate constant ( $k$ ) at 150 and 200 °C.

lysts [17,25,28], and thereby the promoted reducibility of these Ce sites makes them more reactive in NH<sub>3</sub>-SCR reaction. In H<sub>2</sub>-TPR and O<sub>2</sub>-TPD results, there are clear evidences of the strong interaction between Ce<sup>n+</sup> and Nb<sup>n+</sup> at the Nb<sup>n+</sup>—O—Ce<sup>n+</sup> interface. It has been discussed above that NbO<sub>x</sub> species are distributed monolayerly with Nb<sub>2</sub>O<sub>5</sub> loading from 5 wt.% to 15 wt.%. In this case, Nb<sup>n+</sup> may have more opportunities to diffuse into the CZ lattice with increasing Nb<sub>2</sub>O<sub>5</sub> loading amount, leading to generation of more active oxygen species (O<sup>2-</sup>/O<sup>-</sup>) around cerium sites as indicated by the Raman, UV-vis and XPS results.

Some studies in literature [12,21,58,59] reported that the redox property of a catalyst is a key-factor in controlling the reactivity of NH<sub>3</sub>-SCR catalysts at low temperatures. The SCR reaction proceeds firstly via a consumption of active oxygen, then a transferring of lattice oxygen to active sites and subsequently the re-oxidation of reduced catalysts by gas-phase oxygen. In this work, Fig. 14a shows that the amounts of active oxygen, non-active lattice oxygen and capping oxygen from surface NbO<sub>x</sub> estimated by H<sub>2</sub> consumption of Peaks 1–3 in Table S2, respectively. Additionally, Fig. 14b shows the amount of  $\beta$  oxygen species derived from O<sub>2</sub>-TPD measurements in Table S3 as a function of Nb<sub>2</sub>O<sub>5</sub> loading amount. The NO<sub>x</sub> conversions over different catalysts follow the sequence of Nb15CZ > Nb10CZ > Nb20CZ > Nb5CZ > CZ at 150 and 200 °C as shown in Fig. 14c, which is similar to that of amount of active oxygen in H<sub>2</sub>-TPR. This fact indicates that the low-temperature NH<sub>3</sub>-SCR activity is closely correlated with the amount of active oxygen. It is also shown in Fig. 14b that the amount of  $\beta$  oxygen species (O<sub>2</sub><sup>-</sup>, O<sup>-</sup>) calculated from the O<sub>2</sub>-TPD experiment follows the same trend as active oxygen calculated from the H<sub>2</sub>-TPR experiment, although the amount of latter is larger due to the additional contribution of some surface/subsurface lattice oxygen and the different experimental conditions such as existence of reductant (H<sub>2</sub>). The promotion effect of active oxygen on low-temperature activity is probably due to stronger partial oxidation of reactants in the SCR reaction [14,33,35], which is supported by higher NH<sub>3</sub> oxidation and NO oxidation activity on NbCZ catalysts. To further consolidate this, a linear relationship is obtained in Fig. 14d between the amount of active oxygen and the pseudo-first order rate constant ( $k$ ) at 150 and 200 °C, suggesting that the redox property acts as a key factor for the catalytic behaviors at low temperatures. On the other hand, the decrease in the amount of non-active lattice oxygen on CZ after Nb<sub>2</sub>O<sub>5</sub> loading, as shown in Fig. 14a, illustrates that an increasing portion of this inert oxygen can be transformed into active oxygen, which should be associated with the increased oxygen mobility. This increase in oxygen mobility mainly results from more oxygen vacancies after Nb<sub>2</sub>O<sub>5</sub> loading, as they can provide major transfer channels for lattice oxygen (O<sup>2-</sup>) to surface active oxygen (O<sub>2</sub><sup>-</sup>, O<sup>-</sup>) [21,28]. Although the amount of capping oxygen species of NbO<sub>x</sub> also increases with the Nb<sub>2</sub>O<sub>5</sub> content, these oxygen species are relatively inert in the SCR reaction due to the poor redox property indicated by H<sub>2</sub>-TPR results.

In order to discuss the contribution of active sites to the SCR reaction, isothermal reactions were conducted every twenty degrees between 180 and 260 °C. Thus stable and low conversions of NO<sub>x</sub> (<20%) were achieved in an approximate kinetic regime. A much higher gas hourly space velocity (1.2 × 10<sup>6</sup> h<sup>-1</sup>) and less than 200 mesh size powder catalysts were used to achieve kinetically controlled conditions and absence of external mass transport limitations. Fig. 15 shows the Arrhenius plots of the reaction rate for the SCR reaction in the temperature range of 180–260 °C. Within this temperature range, the selectivity to N<sub>2</sub> is close to 100% with no generations of by-products. The apparent activation energies of the SCR reaction for Nb15CZ and CZ are 28.6 kJ mol<sup>-1</sup> and 34.0 kJ mol<sup>-1</sup>, respectively. The reaction pathway of Nb15CZ catalyst should not be changed due to the linear relationship between the pseudo-first

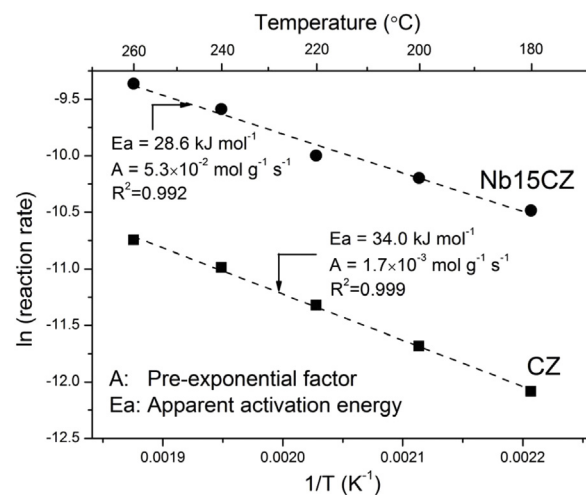


Fig. 15. Arrhenius plots of the reaction rates on CZ and Nb15CZ catalysts. Reaction conditions: [NH<sub>3</sub>] = [NO] = 500 ppm, [O<sub>2</sub>] = 5%, N<sub>2</sub> as balance. GHSV = 1.2 × 10<sup>6</sup> h<sup>-1</sup>.

order rate constant  $k$  and active oxygen amount (Fig. 14d). Therefore, the decrease in apparent activation energy may be related to the improved catalytic reactivity of Ce<sup>n+</sup> sites in the Nb containing catalyst. Furthermore, the pre-exponential factor of Nb15CZ catalyst is 30 times more than that of CZ, indicating a significantly increased number of these active Ce<sup>n+</sup> sites derived from Nb–Ce interaction as evidenced by H<sub>2</sub>-TPR profiles in Fig. 7.

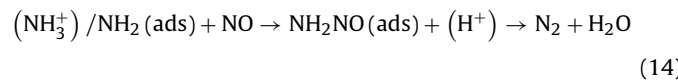
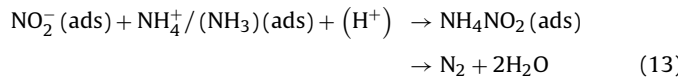
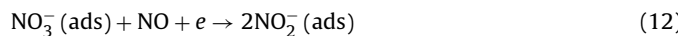
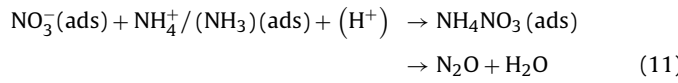
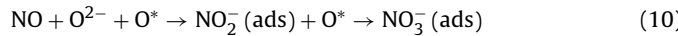
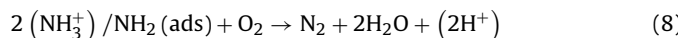
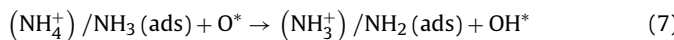
#### 4.3. Reaction mechanism

The surface acidity of the catalyst is also an important factor for SCR reactions at high temperature, which has been proved on mechanisms for different catalysts [11–21,28,35]. Based on our DRIFTS results, the enhanced acidity of NbCZ catalysts is crucial to NH<sub>3</sub> storage, which leads to inhibition of unselective oxidation of ammonia and high N<sub>2</sub> selectivity in NH<sub>3</sub>-SCR reaction [14–21]. NH<sub>2</sub> species are intermediates in ammonia activation and oxidation (Eqs. (7) and (8)) [13–15,19,60], and the increased amount of surface oxygen accelerates the deprotonation of NH<sub>3</sub> to form amide (NH<sub>2</sub>) species. Afterwards, the pre-consumed surface oxygen can be supplemented by gaseous oxygen (Eq. (9)). Since NH<sub>3</sub> always needs to be adsorbed on catalysts and then activated in order to react with gaseous NO<sub>x</sub> [3,4,13], both increased active sites and acid sites are vital to the SCR reaction. Although CZ can also adsorb a large amount of NH<sub>3</sub> as shown in NH<sub>3</sub>-TPD experiment, its SCR activity is quite poor at 200 °C while almost 100% NO<sub>x</sub> conversion is achieved on Nb15CZ. At this temperature, Nb15CZ shows no NH<sub>3</sub> oxidation but noticeable NO oxidation activity, which indicates that NO adsorption and oxidation may be the key factor in determining NH<sub>3</sub>-SCR activity at low temperatures.

The FTIR study of N<sub>x</sub>O<sub>y</sub> adsorption shows that several adsorbed N<sub>x</sub>O<sub>y</sub> species are identified in the DRIFT spectra of CZ and Nb15CZ catalysts. On CZ, NO is supposed to be initially adsorbed on basic Ce<sup>n+</sup>—O<sup>2-</sup> sites, and then stored in form of nitrites and finally oxidized to nitrates (Eq. (10)) [12,16–17,28]. The increased amount of active oxygen accelerates the transformation of nitrites to nitrates at temperatures below 250 °C as shown in Fig. 10b. It can be seen that the thermally stable nitrates (NO<sub>3</sub><sup>-</sup>) cannot participate in the NH<sub>3</sub>-SCR reaction on CZ at low temperatures. They can also occupy the active cerium sites and prohibit the activation of NH<sub>3</sub> [28–30]. However, it is verified by the formation of ammonium nitrate at low temperatures (<350 °C) on Nb15CZ as in Fig. 11b, the SCR reaction over Nb15CZ catalyst is more likely to occur via the Langmuir–Hinshelwood (L–H) mechanism, in which

both the ads-NH<sub>3</sub> and ads-NO<sub>3</sub><sup>−</sup> species participate in the reaction [16,28,35]. The ammonium nitrate is the terminal product only in absence of reducing agent and would decompose to N<sub>2</sub>O and H<sub>2</sub>O (Eq. (11)) [28,35]. When NO is included in the flow gas, ammonium nitrate can be reduced to ammonium nitrite and then decomposed to N<sub>2</sub> and H<sub>2</sub>O (Eqs. (12) and (13)) [28,56]. Considering that almost no N<sub>2</sub>O is generated during the SCR reaction on Nb15CZ catalysts, we can deduct that ammonium nitrates would always transform into ammonium nitrites with continuous NO feeding. All these results indicate that, at low temperatures, ammonium nitrate/nitrite formation may be an important step in the L-H mechanism [9,22,28,35,56]. The large amount of active oxygen facilitates the oxidation of NO on Ce<sup>n+</sup> sites and formation of nitrates at low temperatures, and the acid sites around Ce<sup>n+</sup> sites increase the adsorption of NH<sub>3</sub> species and their opportunities to contact nitrates. Therefore, the reaction of ads-NH<sub>3</sub> with ads-NO<sub>3</sub><sup>−</sup>/NO<sub>2</sub><sup>−</sup> species on Nb15CZ catalyst is promoted in this way.

On the other hand, it is noticeable on Nb15CZ that the stability of nitrates is lowered when raising the temperature above 350 °C. Nb15CZ catalyst containing more active oxygen species which are active for NO to NO<sub>3</sub><sup>−</sup> species transformation can also be active for the reverse reaction, i.e., the dissociation of NO<sub>3</sub><sup>−</sup> species to NO and oxygen sites [61], leading to the instability of nitrates at high temperatures. Apart from this, the enhanced acidity of Nb15CZ is another important factor leading to the reduced stability of surface nitrates. NbO<sub>x</sub> species with Nb=O bonds are electron withdrawing groups, making the catalyst less willing to donate electron pairs to N<sub>x</sub>O<sub>y</sub> species, i.e., reducing the interaction of N<sub>x</sub>O<sub>y</sub> species with catalysts. Therefore, the SCR reaction at high temperatures may follow the Eley–Rideal (E–R) mechanism (Eq. (14)) because of the low participation of the adsorbed nitrate species. The adsorbed NH<sub>3</sub> is firstly partially oxidized to NH<sub>2</sub>, which would subsequently react with NO to form NH<sub>2</sub>NO intermediate and finally generate N<sub>2</sub> and H<sub>2</sub>O [15–18,26–30,60]. The NbO<sub>x</sub> impregnation facilitates the adsorption of ammonia at high temperatures. Meanwhile, the thermal instability of N<sub>x</sub>O<sub>y</sub> species could leave more Ce<sup>n+</sup> sites available for the activation of the adsorbed NH<sub>3</sub> at high temperatures. In this way, the high-temperature activity of Nb15CZ catalysts is greatly promoted.



ads: adsorbed species.

## 5. Conclusions

A series of NbO<sub>x</sub>/CeO<sub>2</sub>–ZrO<sub>2</sub> catalysts, which are synthesized by wetness impregnation methods, show superior NH<sub>3</sub>-SCR activity and selectivity to N<sub>2</sub>. Among them, the catalyst with the Nb<sub>2</sub>O<sub>5</sub> loading of 15 wt.% achieves above 80% NO<sub>x</sub> conversion and nearly 100% N<sub>2</sub> selectivity within a broad operation temperature window (190–460 °C) under a high space velocity (3 × 10<sup>5</sup> h<sup>−1</sup>). Several conclusions with regard to surface acidity, redox property and reaction mechanism are drawn as below.

(1) Altering the niobia loading amount would lead to evolution in the structure and distribution of surface supported NbO<sub>x</sub> species and variation of electronic interaction between Nb and the CZ support. The electron transfer effect from Nb<sup>n+</sup> to Ce<sup>n+</sup> would lead to increased amounts of Ce<sup>3+</sup>, oxygen vacancies and active oxygen.

(2) The total surface acidity of the catalyst is remarkably enhanced upon niobia loading, which could promote NH<sub>3</sub> adsorption and prevent the unselective oxidation of NH<sub>3</sub>. This is especially favorable to SCR the reaction at high temperatures (>300 °C). The increase in the amount and strength of acidity is ascribed to the addition of NbO<sub>x</sub> species and their strong withdrawing effect with CZ support.

(3) The increased amount of cerium sites with adjacent active oxygen contributes to the high catalytic activity on NbCZ catalysts, especially at low temperatures. This is achieved by the enhanced NH<sub>3</sub> activation and NO<sub>3</sub><sup>−</sup> formation, and the subsequent promoted reaction of ads-NH<sub>3</sub> and ads-NO<sub>3</sub><sup>−</sup>/NO<sub>2</sub><sup>−</sup> species according to the Langmuir–Hinshelwood mechanism. At high temperatures, the thermal stability of the adsorbed NO<sub>3</sub><sup>−</sup> species are reduced significantly, and thus the SCR reaction on this catalyst mainly follows the Eley–Rideal mechanism via the reaction of ads-NH<sub>2</sub> species and gaseous NO.

## Acknowledgements

The authors would like to acknowledge the National Science Foundation for the financial support of Projects (No. 51202126 and 51372137) and the Ministry of Science and Technology, PR China for financial support of Project 2013AA065302.

## Appendix A. Supplementary data

Supplementary data associated with this article can be found, in the online version, at <http://dx.doi.org/10.1016/j.apcatb.2015.05.038>

## References

- [1] K. Skalska, J.S. Miller, S. Ledakowicz, *Sci. Total Environ.* 408 (2010) 3976–3989.
- [2] L. Lietti, I. Nova, P. Forzatti, *Top. Catal.* 11/12 (2000) 111–122.
- [3] G. Busca, L. Lietti, G. Ramis, F. Berti, *Appl. Catal. B: Environ.* 18 (1998) 1–36.
- [4] F. Liu, Y. Bo, H. He, *Chem. Commun.* 50 (2014) 8445–8463.
- [5] J.P. Dunn, P.R. Koppula, H.G. Stenger, I.E. Wachs, *Appl. Catal. B Environ.* 19 (1998) 103–117.
- [6] S. Shwan, J. Jansson, L. Olsson, M. Skoglundh, *Appl. Catal. B Environ.* 166–167 (2015) 277–286.
- [7] S. Shwan, R. Nedalkova, J. Jansson, J. Korsgren, L. Olsson, M. Skoglundh, *Ind. Eng. Chem. Res.* 51 (2012) 12762–12772.
- [8] X. Gao, Y. Jiang, Y. Fu, Y. Zhong, Z. Luo, K. Cen, *Catal. Commun.* 11 (2010) 465–469.
- [9] W. Xu, H. He, Y. Yu, *J. Phys. Chem. C* 113 (2009) 4426–4432.
- [10] W. Xu, Y. Yu, C. Zhang, H. He, *Catal. Commun.* 9 (2008) 1453–1457.
- [11] L. Chen, J. Li, M. Ge, R. Zhu, *Catal. Today* 153 (2010) 77–83.
- [12] Y. Peng, K. Li, J. Li, *Appl. Catal. B: Environ.* 140–141 (2013) 483–492.
- [13] Z. Ma, D. Weng, X. Wu, Z. Si, *J. Environ. Sci. -China* 24 (2012) 1305–1316.
- [14] W. Shan, F. Liu, H. He, X. Shi, C. Zhang, *Appl. Catal. B Environ.* 115–116 (2012) 100–106.
- [15] W. Shan, F. Liu, H. He, X. Shi, C. Zhang, *Chem. Commun.* 47 (2011) 8046–8048.
- [16] L. Chen, J. Li, M. Ge, *Environ. Sci. Technol.* 44 (2010) 9590–9596.
- [17] Y. Peng, Z. Liu, X. Niu, L. Zhou, C. Fu, H. Zhang, J. Li, W. Han, *Catal. Commun.* 19 (2012) 127–131.

[18] Y. Peng, K. Li, J. Li, *Appl. Catal. B Environ.* 140–141 (2013) 483–492.

[19] T. Gu, Y. Liu, X. Weng, H. Wang, Z. Wu, *Catal. Commun.* 12 (2010) 310–313.

[20] Z. Si, D. Weng, X. Wu, J. Yang, B. Wang, *Catal. Commun.* 11 (2010) 1045–1048.

[21] Z. Si, D. Weng, X. Wu, Z. Ma, J. Ma, R. Ran, *Catal. Today* 201 (2013) 122–130.

[22] M. Casapu, O. Kröcher, M. Elsener, *Appl. Catal. B Environ.* 88 (2009) 413–419.

[23] M. Casapu, O. Kröcher, M. Mehrling, M. Nachtegaal, C. Borca, M. Harfouche, D. Grolimund, *J. Phys. Chem. C* 114 (2010) 9791–9801.

[24] M. Casapu, A. Bernhard, D. Peitz, M. Mehrling, M. Elsener, O. Kröcher, *Appl. Catal. B Environ.* 103 (2011) 79–84.

[25] R. Qu, X. Gao, K. Cen, J. Li, *Appl. Catal. B Environ.* 142–143 (2013) 290–297.

[26] Z. Ma, D. Weng, X. Wu, Z. Si, B. Wang, *Catal. Commun.* 27 (2012) 97–100.

[27] Z. Si, D. Weng, X. Wu, R. Ran, Z. Ma, *Catal. Commun.* 17 (2012) 146–149.

[28] J. Yu, Z. Si, L. Chen, X. Wu, D. Weng, *Appl. Catal. B Environ.* 163 (2015) 223–232.

[29] Z. Liu, S. Zhang, J. Li, L. Ma, *Appl. Catal. B Environ.* 144 (2014) 90–95.

[30] J. Zhu, F. Gao, L. Dong, W. Yu, L. Qi, Z. Wang, L. Dong, Y. Chen, *Appl. Catal. B Environ.* 95 (2010) 144–152.

[31] R. Braynera, D. Ciuparu, G.M.d. Cruzb, F. Fiévet-Vincenta, F. Bozon-Verduraza, *Catal. Today* 57 (2000) 261–266.

[32] K. Yashiro, T. Suzuki, A. Kaimai, H. Matsumoto, Y. Nigara, T. Kawada, J. Mizusaki, J. Sfeir, J.V. herle, *Solid State Ionics* 175 (2004) 341–344.

[33] Y. Wei, J. Liu, Z. Zhao, A. Duan, G. Jiang, *J. Catal.* 287 (2012) 13–29.

[34] R. Si, Y. Zhang, S. Li, B. Lin, C. Yan, *J. Phys. Chem. B* 108 (2004) 12481–12488.

[35] J. Li, H. Chang, L. Ma, J. Hao, R.T. Yang, *Catal. Today* 175 (2011) 147–156.

[36] B.M. Reddy, A. Khan, Y. Yamada, T. Kobayashi, S. Loridan, J.-C. Volta, *J. Phys. Chem. B* 107 (2003) 11475–11484.

[37] B.M. Reddy, A. Khan, Y. Yamada, T. Kobayashi, S. Loridan, J.-C. Volta, *Langmuir* 19 (2003) 3025–3030.

[38] I. Kosacki, T. Suzuki, H.U. Anderson, P. Colombari, *Solid State Ionics* 149 (2002) 99–105.

[39] M.A. Bañares, I.E. Wachs, *J. Raman Spectrosc.* 33 (2002) 359–380.

[40] I. Nowak, M. Ziolek, *Chem. Rev.* 99 (1999) 3603–3624.

[41] L.J. Burcham, J. Datka, I.E. Wachs, *J. Phys. Chem. B* 103 (1999) 6015–6024.

[42] O.C. Compton, F.E. Osterloh, *J. Phys. Chem. C* 113 (2009) 479–485.

[43] M. Mączka, M. Ptak, A. Majchrowski, J. Hanuza, *J. Raman Spectrosc.* 42 (2011) 209–213.

[44] D. Terribilea, A. Trovarellia, J. Llorcab, C. d. Leitenburga, G. Dolcettia, *Catal. Today* 43 (1998) 79–88.

[45] X. Du, L. Dong, C. Li, Y. Liang, Y. Chen, *Langmuir* 15 (1999) 1693–1697.

[46] S. Tsunekawa, T. Fukuda, *J. Appl. Phys.* 87 (1999) 1318–1321.

[47] E. Bêche, P. Charvin, D. Perarnau, S. Abanades, G. Flamant, *Surf. Interface Anal.* 40 (2008) 264–267.

[48] X. Du, X. Gao, Y. Fu, F. Gao, Z. Luo, K. Cen, *J. Colloid Interface Sci.* 368 (2012) 406–412.

[49] A. Lewandowska, M. Banares, *Catal. Today* 118 (2006) 323–331.

[50] S. Pengpanich, V. Meeyoo, T. Rirkosomboon, J. Schwank, *J. Nat. Gas Chem.* 16 (2007) 227–234.

[51] Li K. Li, H. Wang, Y. Wei, M. Liu, *J. Rare Earths* 26 (2008) 705–710.

[52] D. Sun, Q. Liu, Z. Liu, G. Gui, Z. Huang, *Appl. Catal. B: Environ.* 92 (2009) 462–467.

[53] T. Onfroy, G. Clet, M. Houalla, *J. Phys. Chem. B* 109 (2005) 14588–14594.

[54] M. Adamowska, A. Krztoń, M. Najbar, P. Da Costa, G. Djéga-Mariadassou, *Catal. Today* 137 (2008) 288–291.

[55] K.I. Hadjivanov, *Catal. Rev.* 42 (2000) 71–144.

[56] I. Nova, C. Ciardelli, E. Tronconi, D. Chatterjee, B. Bandl-Konrad, *Catal. Today* 114 (2006) 3–12.

[57] J. Zhu, L. Zhang, Y. Deng, B. Liu, L. Dong, F. Gao, K. Sun, L. Dong, Y. Chen, *Appl. Catal. B Environ.* 96 (2010) 449–457.

[58] P.W. Seo, S.P. Cho, S.H. Hong, S.C. Hong, *Appl. Catal. A General* 380 (2010) 21–27.

[59] L. Lietti, P. Forzatti, F. Berti, *Catal. Lett.* 41 (1996).

[60] G. Ramis, L. Yi, G. Busca, M. Turco, E. Kotur, R.J. Willey, *J. Catal.* 157 (1995) 523–535.

[61] I. Atribak, B. Azambre, A. Bueno López, A. García-García, *Appl. Catal. B Environ.* 92 (2009) 126–137.